

AWARD NUMBER: W81XWH-13-1-0341

TITLE: "Delivery of Nano-Tethered Therapies to Brain Metastases of Primary Breast Cancer Using a Cellular Trojan Horse"

PRINCIPAL INVESTIGATOR: Susan E Clare, MD, PhD

CONTRACTING ORGANIZATION: Northwestern University
Evanston, IL 60208

REPORT DATE: October 2015

TYPE OF REPORT: Annual

PREPARED FOR: U.S. Army Medical Research and Materiel Command
Fort Detrick, Maryland 21702-5012

DISTRIBUTION STATEMENT: Approved for Public Release;
Distribution Unlimited

The views, opinions and/or findings contained in this report are those of the author(s) and should not be construed as an official Department of the Army position, policy or decision unless so designated by other documentation.

REPORT DOCUMENTATION PAGE				Form Approved OMB No. 0704-0188	
Public reporting burden for this collection of information is estimated to average 1 hour per response, including the time for reviewing instructions, searching existing data sources, gathering and maintaining the data needed, and completing and reviewing this collection of information. Send comments regarding this burden estimate or any other aspect of this collection of information, including suggestions for reducing this burden to Department of Defense, Washington Headquarters Services, Directorate for Information Operations and Reports (0704-0188), 1215 Jefferson Davis Highway, Suite 1204, Arlington, VA 22202-4302. Respondents should be aware that notwithstanding any other provision of law, no person shall be subject to any penalty for failing to comply with a collection of information if it does not display a currently valid OMB control number. PLEASE DO NOT RETURN YOUR FORM TO THE ABOVE ADDRESS.					
1. REPORT DATE October 2015		2. REPORT TYPE Annual		3. DATES COVERED 15 Sep 2014 - 14 Sep 2015	
4. TITLE AND SUBTITLE "Delivery of Nano-Tethered Therapies to Brain Metastases of Primary Breast Cancer Using a Cellular Trojan Horse"				5a. CONTRACT NUMBER	
				5b. GRANT NUMBER W81XWH-13-1-0341	
				5c. PROGRAM ELEMENT NUMBER	
6. AUTHOR(S) Susan E Clare, MD, PhD E-Mail: susan.clare@northwestern.edu				5d. PROJECT NUMBER	
				5e. TASK NUMBER	
				5f. WORK UNIT NUMBER	
7. PERFORMING ORGANIZATION NAME(S) AND ADDRESS(ES) Northwestern University 633 Clark Street Evanston, IL 60208-0001				8. PERFORMING ORGANIZATION REPORT NUMBER	
9. SPONSORING / MONITORING AGENCY NAME(S) AND ADDRESS(ES) U.S. Army Medical Research and Materiel Command Fort Detrick, Maryland 21702-5012				10. SPONSOR/MONITOR'S ACRONYM(S)	
				11. SPONSOR/MONITOR'S REPORT NUMBER(S)	
12. DISTRIBUTION / AVAILABILITY STATEMENT Approved for Public Release; Distribution Unlimited					
13. SUPPLEMENTARY NOTES					
14. ABSTRACT The purpose of this work is to utilize monocyte/macrophage-enabled delivery, a novel therapeutic delivery system that we pioneered, to increase the effectiveness and decrease the toxicity of the treatment of intracranial metastases from primary breast cancer. Our objective in this proposal is to deliver therapeutics to brain metastases using a nanoshell (NS)-double-stranded DNA (dsDNA)-drug complex loaded within monocytes/macrophages. Once present within the metastasis, we aim to release the drug by transcranial irradiation at near-infrared (NIR) wavelengths. Our studies have provided fundamental information on a number of aspects of the delivery of therapeutics by NSdsDNA. 1. It is of key importance that the therapeutic is soluble and stable in aqueous solution; 2. Dehybridization of DNA duplexes on the nanoshell surface is a thermal phenomenon. 3. Although doxorubicin is a DNA intercalating agent, it may distort the double helix such that it is not a secure cargo. 4. We have estimated, to the best of our knowledge for the first time, the amount and distribution of near infrared light able to be delivered through the skull and brain tissue.					
15. SUBJECT TERMS					
16. SECURITY CLASSIFICATION OF:			17. LIMITATION OF ABSTRACT Unclassified	18. NUMBER OF PAGES	19a. NAME OF RESPONSIBLE PERSON USAMRMC
a. REPORT Unclassified	b. ABSTRACT Unclassified	c. THIS PAGE Unclassified			19b. TELEPHONE NUMBER (include area code)

Table of Contents

	<u>Page</u>
1. Introduction.....	4
2. Keywords.....	4
3. Overall Project Summary.....	4-14
4. Key Research Accomplishments.....	14-15
5. Conclusion.....	15-16
6. Publications, Abstracts, and Presentations.....	16
7. Inventions, Patents and Licenses.....	16
8. Reportable Outcomes.....	17
9. Other Achievements.....	17
10. References.....	17-18
11. Appendices.....	19-42

1. INTRODUCTION: The blood-brain barrier renders the central nervous system a sanctuary site for disease. In the era prior to the development of effective systemic therapies this fact was not of much clinical relevance as most patients succumbed to visceral metastatic disease before their brain metastases became symptomatic. However, as systemic breast cancer therapies improve and are able to successfully control non-Central Nervous System Disease, the brain is increasingly the first site of relapse. Both conventional chemotherapeutic agents and targeted monoclonal antibodies do not cross the blood-brain barrier (BBB) at concentrations sufficient to successfully treat metastatic disease. The objective of the proposed work is to use an active form of transport of therapeutics across the BBB; a transport mechanism that does not rely on passive diffusion or receptor-mediated transcytosis. We hypothesize that monocytes/macrophages are actively recruited to metastases by cytokines elaborated by the tumors and that these cells can be utilized to transport therapeutics directly to brain metastases of breast cancer. This hypothesis is supported by a pilot study we published that demonstrated delivery in a mouse model of fluorescent microspheres to brain metastases by macrophages.⁽¹⁾ Our objective in this proposal is to deliver a therapeutic, doxorubicin, to brain metastases using a nanoshell-double-stranded DNA (dsDNA)-drug complex loaded within monocytes/macrophages. Once present within the metastasis, we aim to release the drug by transcranial irradiation at near-infrared (NIR) wavelengths.

2. KEYWORDS: *Brain metastases, nanoshells, macrophage, monocyte, blood-brain barrier, photothermal therapy, light triggered release, Adriamycin, doxorubicin, metastatic breast cancer, Trojan horse*

3. OVERALL PROJECT SUMMARY: *Summarize the progress during appropriate reporting period (single annual or comprehensive final). This section of the report shall be in direct alignment with respect to each task outlined in the approved SOW.*

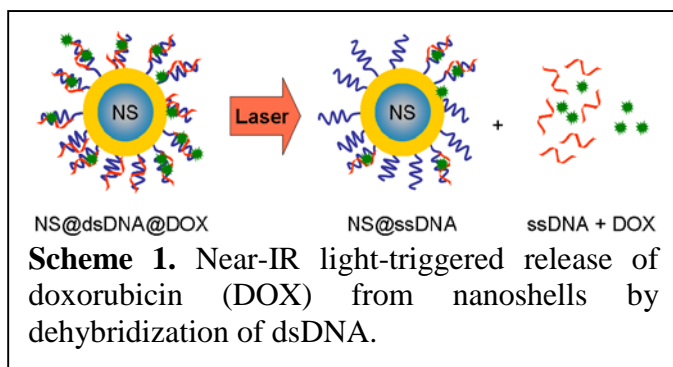
Task 1

a. *Current objectives*

The original proposal suggested the immobilization and near-IR triggered delivery of lapatinib from gold nanoshells. The goal was to load lapatinib onto the nanoshell surface through the intercalation of dsDNA sequences bound to the nanoshell surface. The dsDNA sequences would have one strand that was thiolated and covalently linked to the particle surface, while the complementary strand was not. Upon irradiation, the complementary sequence would be released from the particle surface thereby releasing lapatinib locally. We proposed to load these nanocomplexes into macrophage / monocyte cells that could then be used to deliver them into the brain metastases.

In last year's report, we detailed the difficulties we encountered with lapatinib solubility and light-triggered release. As a potential solution, we decided to focus on the delivery of doxorubicin (DOX). DOX is a

chemotherapeutic agent, used in the conventional treatment of cancers including: Hodgkin's lymphoma, myeloma, lung, ovarian, gastric, thyroid, breast, sarcoma, and pediatric cancers. Its mechanism of action is to intercalate between the double strands of DNA. Our modified approach is to intercalate DOX into a GC rich double-stranded DNA (dsDNA) sequence and under laser

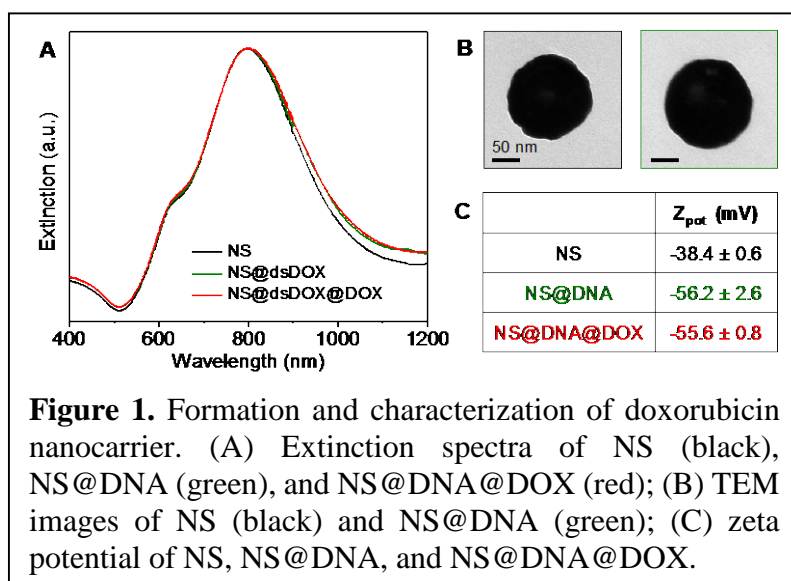


illumination at the plasmon resonance of the NS@DNA@DOX complex, dehybridize the dsDNA and release DOX (Scheme 1).

b. Results

In order to deliver DOX, we synthesized a nanocarrier from which DOX could be released by DNA dehybridization. The dsDNA sequences used in this study were engineered specifically to bind to the chemotherapeutic DOX: 5'-HS-(CH₂)₆-CAA TCA ATA GCT ATC GTT CG-3' and 3'-GTT AGT TAT CGA TAG CAA GC-5'. Prior to attachment to the nanoshell (NS) surface the DNA was hybridized by mixing equal moles of the two DNA strands with 33 mM NaCl, heating the mixture to 100 °C for 4 min and slowly cooling to room temperature overnight. Nanoshells were functionalized with double-stranded DNA (dsDNA) via a Au-S bond. The dsDNA-NS mixture was incubated overnight with continuous shaking. The solution was washed several times to remove the dsDNA excess. The NS@dsDNA complex was incubated with DOX for 24 h and excess DOX was removed via centrifugation.

Vis-NIR spectroscopy, transmission electron microscopy (TEM), zeta potential, and dynamic light scattering (DLS) measurements were utilized to provide evidence of the formation of the DOX nanocarrier. The extinction maximum of bare NS slightly red-shifted after dsDNA functionalization, due to the change in the dielectric environment around the NS (Fig. 1A). No changes in the peak shape or width of the extinction spectra was observed, indicating that the NS@dsDNA nanocomplexes do not aggregate during the functionalization process. TEM images



illustrate the thin layer of DNA formed on the nanoshell surface (Fig. 1B). Zeta potential measurements further confirm modification of the NS surface (Figure 1C). The zeta potential of the particles decreased ~18 mV after

DNA functionalization as a result of the negative charges on the DNA phosphate backbone. The zeta potential increased slightly after incubation with DOX due to screening of the DNA charges.

Cellular uptake of the NS@DNA complex was investigated using confocal and reflectance (emission and excitation at 640 nm) microscopy. For the initial experiments, RAW 264.7 a mouse macrophage cell line from an Abelson murine leukemia virus-induced tumor is being. This cell line has the advantage of being immortalized and is easy to propagate in cell culture in comparison to the monocytes isolated from human blood and utilized previously. Briefly, the RAW 264.7 macrophage cells were cultured for 24 h in a μ -Slide 8- well and then incubated with the NS@dsDNA. After 20 h, the cells were rinsed three times with PBS and fixed in a 4% paraformaldehyde solution. The cells were washed twice with PBS and incubated with a Hoechst 33342 solution to stain the cell nucleus. After 10 min of incubation and protected from light, the cells were rinsed twice with PBS. All images were collected on a Nikon A1-Rsi Confocal microscope and the particles were imaged in the reflection mode. The 3D maximum intensity projection image, corresponding to a slice from the middle of the cell, confirms internalization of the NS@DNA nanoparticles (red dots, Fig. 2). The details in the orthogonal YZ and XZ planes illustrate the location of the nanoparticles within the cell boundary, around but not inside the nucleus.

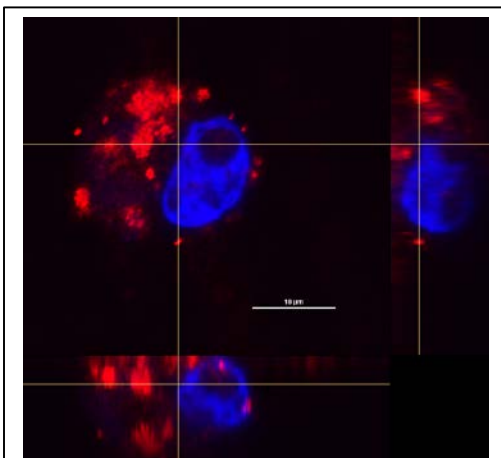


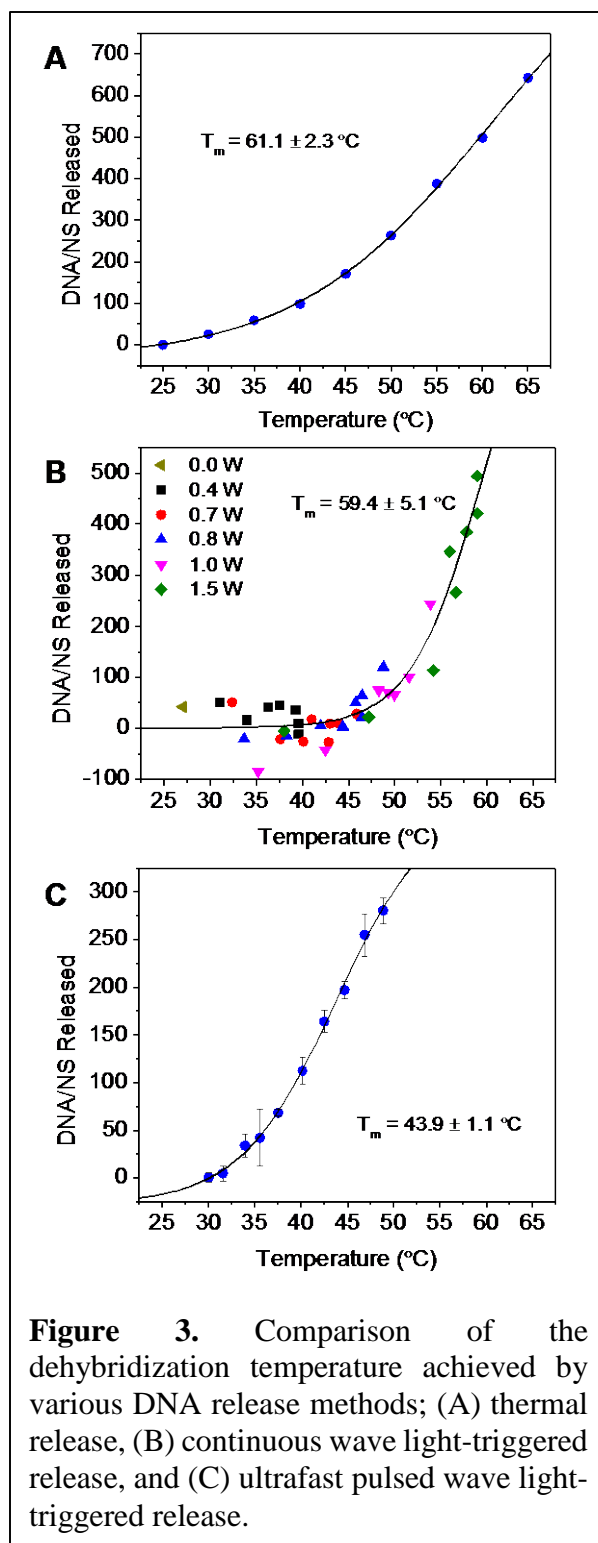
Figure 2. Confocal image of cellular uptake of the nanoshell-DNA nanocomplex in a RAW 264.7 macrophage cell. Orthogonal view of the 3D maximum intensity projection image of cells incubated overnight with nanocarrier. Nucleus is stained blue with Hoechst 33342. Nanoparticles were located by reflection (emission and extinction at 640 nm). Scale bar = 10 μ m; 60x oil immersion objective; NA = 1.4.

In response to the previous challenges we encountered with regard to demonstrating light-triggered release of lapatinib, we decided to take a step back and investigate in greater detail the mechanism of light-triggered release in order to better control and tailor the release for various molecular cargos. In this study, we used NS functionalized with dsDNA; one strand was thiolated and the complementary strand tagged with fluorescein [5'HS-(CH₂)₆-TAT GAT CTG TCA CAG CTT GA-3' and 5'- ATA CTA GAC AGT GTC GAA CT-Fluor-3']. The dsDNA dehybridization process was investigated by fluorescence spectroscopy. It had previously been demonstrated that when a high concentration of nanoparticles was present, release of cargo using a continuous wave (CW) laser could be achieved at temperatures below the DNA dehybridization temperature [1]. Based on this observation, a non-thermal release mechanism by hot-electrons was proposed. In this study, we reduced the particle concentration to better simulate the concentration of particles that is realistically achievable within a tumor. We found by heating the nanoparticle solution with a temperature-controlled stage that thermally induced dehybridization of our specific dsDNA sequence occurred at 61.1 ± 2.3 °C (Fig. 3A). Dehybridization of the same

sequence using CW light occurred at 59.4 ± 5.1 °C (Figure 3B). In these experiments, we observed that release does not occur until the laser power is high enough to increase the bulk temperature above the dehybridization temperature. This is evidence that the dsDNA dehybridization occurs as a result of the heating from the nanoparticles as opposed to hot-electrons, which would be linearly dependent on the laser power. The high nanoparticle concentrations used in earlier experiments resulted in optical light trapping due to multiple scattering of the nanoparticles, allowing the local temperature to increase and dehybridize the DNA before a significant rise in the global/bulk temperature was measured. Unfortunately, that nanoparticle concentration is not achievable in a tumor. Alternatively, a femtosecond pulsed wave laser enables significant temperature increases on the nanoparticle surface without heating the solution (Figure 3C). By irradiating our nanoparticle solution with an ultrafast laser, we were able to demonstrate release at 43.9 ± 1.1 °C, ~ 16 °C below the dehybridization temperature. By further decreasing the spot size, we should be able to release the DNA without any measureable temperature increase.

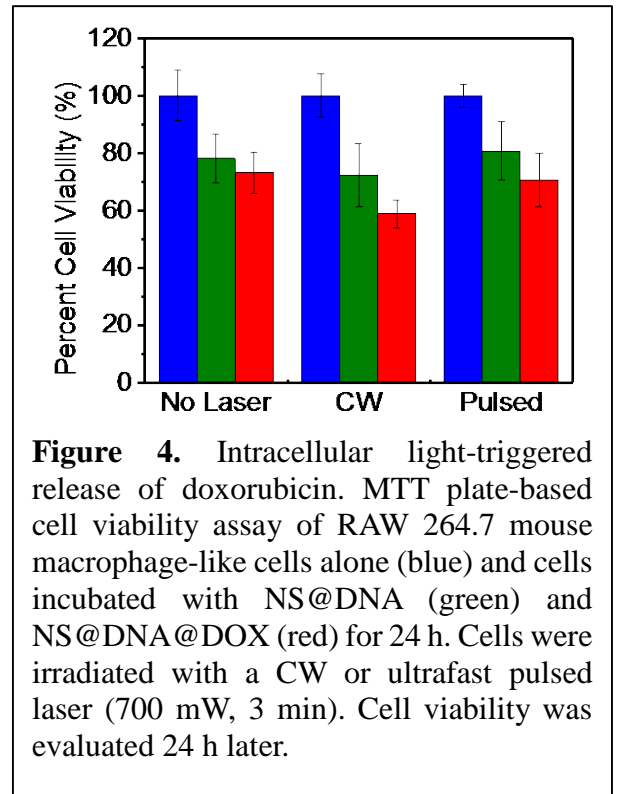
Subsequently, we examined the intracellular release of DOX by both CW and pulsed lasers. An MTT [3-(4,5-dimethylthiazol-2-yl)-2,5-diphenyltetrazolium bromide] cell proliferation assay was performed to investigate both the effects of the nanocarrier and laser irradiation on cell viability. RAW 264.7 macrophage cells were used for the cytotoxicity studies. All experiments were performed in triplicate and the percentages of viable cells were calculated considering the absorbance of the control well as a 100% live cells. The DOX nanocarrier was incubated with cells overnight, and then irradiated at 700 mW for 3 min. The cell proliferation assay was performed at 24 h.

In all studies, an increase in cell death was observed for the DOX nanocarrier when compared to cells with the NS-DNA nanocomplex (Fig. 4). However, the same amount of cell death was observed for the cells with the unilluminated DOX nanocarrier as for the cells with the DOX nanocarrier illuminated with the CW or pulsed



laser. This result suggests that the DOX may be leaking out of the complex before irradiation. It is theoretically possible but unlikely that the DOX nanocarrier is toxic to the cells. We have previously shown that a similar nanocarrier loaded with DAPI is not toxic to cells [2].

Current and future objectives include studies to determine if DOX is leaking out of the DNA, selection of an alternate drug that can be maintained within the dsDNA@NS complex until release is triggered and development of a new host (i.e. peptides) for the DOX light triggered release process.



Task 2

a. Current objective

To optically release the drug attached to the surface of the gold nanoparticle, it is necessary to deliver and validate the *instantaneous* fluence (the radiant energy per unit surface area) at the location of the tumor. Given that, there is little data on the amount and distribution of near infrared light through the skull and brain tissue. To provide an estimate of the energy transport of near infrared light through the skull and within brain tissue, a number of diagnostic tools were developed. First, a nearly isotropic optical dosimetry probe was fabricated to obtain local photon fluence measurements with 1.5 mm spatial resolution and high sensitivity. Calibration of the probe was performed in air and water-based phantoms using a calorimeter (considered a Gold Standard). Second, a voxel-based Monte Carlo simulation code written in CUDA for GTX Nvidia (Dr. Fang, Harvard) was further developed for different optical beam properties, such as super Gaussian beams with parallel, converging, and diverging beam profiles, and with the ability to run on multiple Nvidia cards (n=3). Third, an empirical method to simulate photon transport was developed to provide sufficiently accurate solution at accelerated rates. Monte Carlo simulations for photon transport are computational intensive and therefore are typically not practical for clinical use. These codes provide solutions in real-time during the developmental stage of the treatment plan. These tools were used to:

2a. Estimate of the attenuation of near infrared irradiation by the skull using the fluence probe; and

2b. Estimate of the attenuation of near infrared irradiation by the skull and brain tissue phantom using the fluence probe.

b. Results

i. Calibration of the Optical Dosimetry Probe (ODP) [1,3]: The objective was to fabricate and calibrate the optical dosimetry probe (ODP) to a calorimeter (Nova II; Ophir). The ODP consists of a 1.5 mm diameter sphere (epoxy and titanium dioxide) molded onto the end of a 200 μ m optical fiber. The output of the fiber was coupled to a photodiode (ET-2030, Electro Optics Technology Inc), the output of which was recorded by a digital oscilloscope (Tektronix TDS3052B). The digitized signal was uploaded to a PC, where the signal was passed through a high-pass butterworth filter to reduce background noise and the area underneath the pulse calculated to determine the photon fluence. To calibrate the ODP, the photon fluence in air was measured by both the ODP and calorimeter using a uniform laser beam formed by passing the output of the laser/OPO system (Nd:YAG class 4 laser/ MagicPRISM OPO, Opotek Inc.) (tuned to 800nm) through an integrating sphere (Melles Griot). The results are displayed in Figure 1. To determine the fluence in water (or tissue), the change in the index of refraction causes the reflective properties between the probe media and water to change, thus requiring an additional correction factor. The probe was placed within a macrocuvette, a plexiglass container which was approximately 5.0 x 5.0 x 5.0 cm³ (5mm thick walls). The ODP signal and calorimeter measurements were acquired in air as before. The macrocuvette was then filled with water, and the ODP was positioned along the central axis of the uniform beam. From this data, a conversion factor was applied to the ODP signal to convert the calibration curves in air (Figure 1) to tissue. This conversion factor also took into account the variation in the beam width when traversing from plexiglass-to-air versus plexiglass-to-water and photon attenuation for optical path lengths within water, both of which were relative small (~3%, the average error in the laser output power).

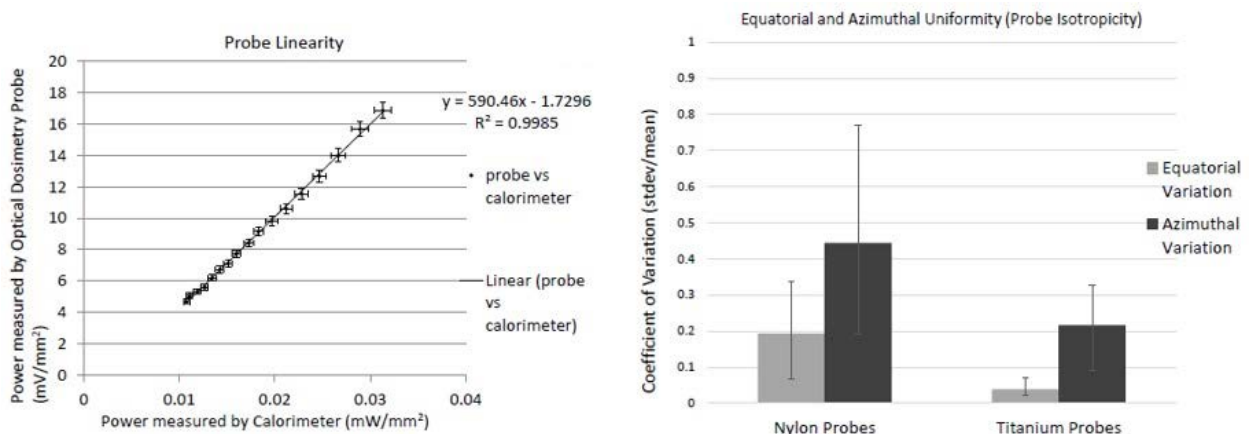


Figure 1: (Left) The output of the ODP in mVolts plotted as a function of laser fluence measured by a calorimeter. **(Right)** The angular dependency (azimuthal and rotation) of the ODP to the direction of laser light was calculated as a function of the absolute value of the residuals and how it compares to nylon probes.

ii. Phantoms Reproducing the Optical Properties of the Head: The objective was to develop a formula that could be used to create water-based (and agar-based) phantoms with the desired optical properties (μ_a and μ_s')

for the skull, white matter and gray matter (at 800nm, the wavelength of stimulated drug release). India ink was used as the absorber (with some but little scattering), while intralipid was used as a scatterer (with some but little absorption). To determine the absorption coefficient, various concentrations of india ink in water were placed within the photospectrometer, from which a calibration curve plotted: $15.07 \times \% (\text{india ink}) + 0.0049$ ($r^2=0.99$) (data not shown). The reduced scattering coefficient was determined by placing different concentrations (from 1 to 7%) of intralipid in water, exposing the solution to a uniform (1cm diameter) laser beam using an integrating sphere as described in the previous section. The photon fluence was measured using the ODP at various path lengths (or depths) along the central axis of the beam. To determine the reduced scattering coefficient in each sample, Monte Carlo simulations were performed for various reduced scattering coefficients until a minimum in the chisquare was reached. The data was plotted and fit to a line: $11.30 \times (\% \text{ intralipid}) - 2.17$ ($r^2=0.99$) (data not shown). From these measurements, the white and gray matter phantoms were fabricated based the optical properties

Table I: Optical properties of the skull bone, white matter, and gray matter.

	μ_a	μ_s	g	μ_s'	intralipid	ink
	[cm^{-1}]	[cm^{-1}]		[cm^{-1}]	[%]	[%]
white	0.05	550	0.85	82.5	7.5	0
gray	0.35	700	0.965	24.5	2.36	0.023
skull	0.24	184	0.9	18.4	1.82	0.0156

measured by Van der Zee et al [6], and the skull phantom optical properties were based on measurements by Firbank et al [7], see Table I.

iii. **Simulating Photon Transport in Phantoms/Tissue** [1-3]: The objective was to develop and validate a voxel-based Monte Carlo code of photon transport in the head and brain. A voxel-based 3-D Monte Carlo (MC) code (Fang et al [8]) developed in CUDA for NVidia cards was modified to allow the user to create laser sources with various aperture profiles, such as uniform and super-Gaussian, and directionality, such as diffusive, converging, and diverging beams. Supporting code (Matlab) was developed to allow the user to design their own objects, which in this study was based on phantom designs and medical images (CT).

A critical advantage of a voxel-based code is not only to include tissue heterogeneities but to integrate medically acquired images into the simulations. To date, the MC code has not been validated with measured data; therefore, a number of experiments were performed. First, the photon fluence distribution was measured using the ODP in phantoms representing white matter, gray matter, and skull bone. The ODP probe was secured to a 3-D stage micrometer to obtain measurements along the central axis of the beam at various depths in the phantom (axial profile) and perpendicular to the central axis (lateral profile). These measurements were taken using a uniform

and a super Gaussian laser beam. Next, Monte Carlo simulations were performed and compared to measurement. In Figure 2, the normalized fluence along the central axis of the flat beam was plotted for both white and gray and for ODP and MC data. For depths up to 2 cm, the agreement is within 3%. Similar experiments were performed for the super Gaussian beam, where for depths up to 3 cm, the MC simulated results

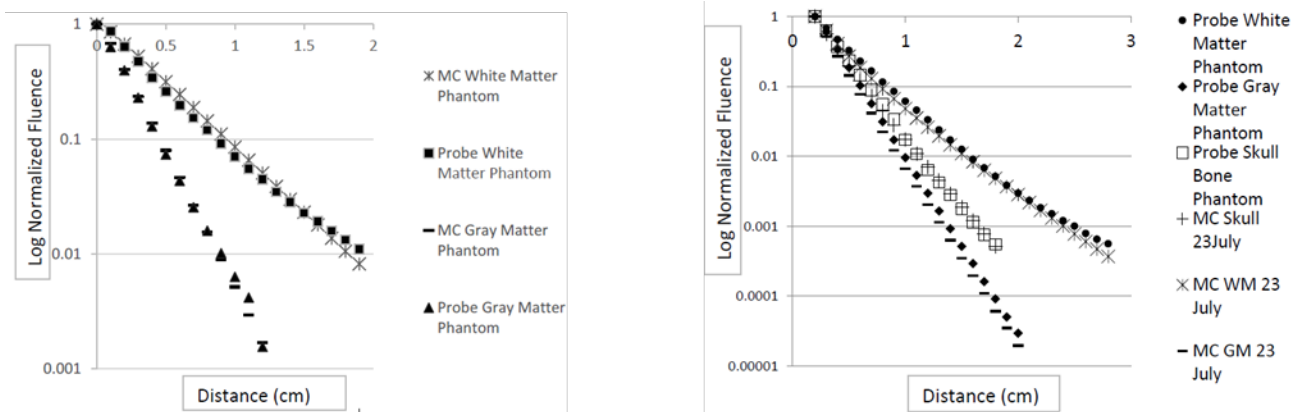


Figure 2. The fraction of the input fluence as measured by the ODP at different depths in white and gray matter phantoms for a uniform laser beam (1.0cm in diameter) (*left*) and a super Gaussian beam profile (*right*). Included in these plots are the Monte Carlo simulated results, which agree to within 3.0% of the measured values.

matched the ODP measurements. The comparison of the lateral profiles for the super Gaussian beam is shown in Figure 3, and demonstrates the excellent agreement between ODP and MC results.

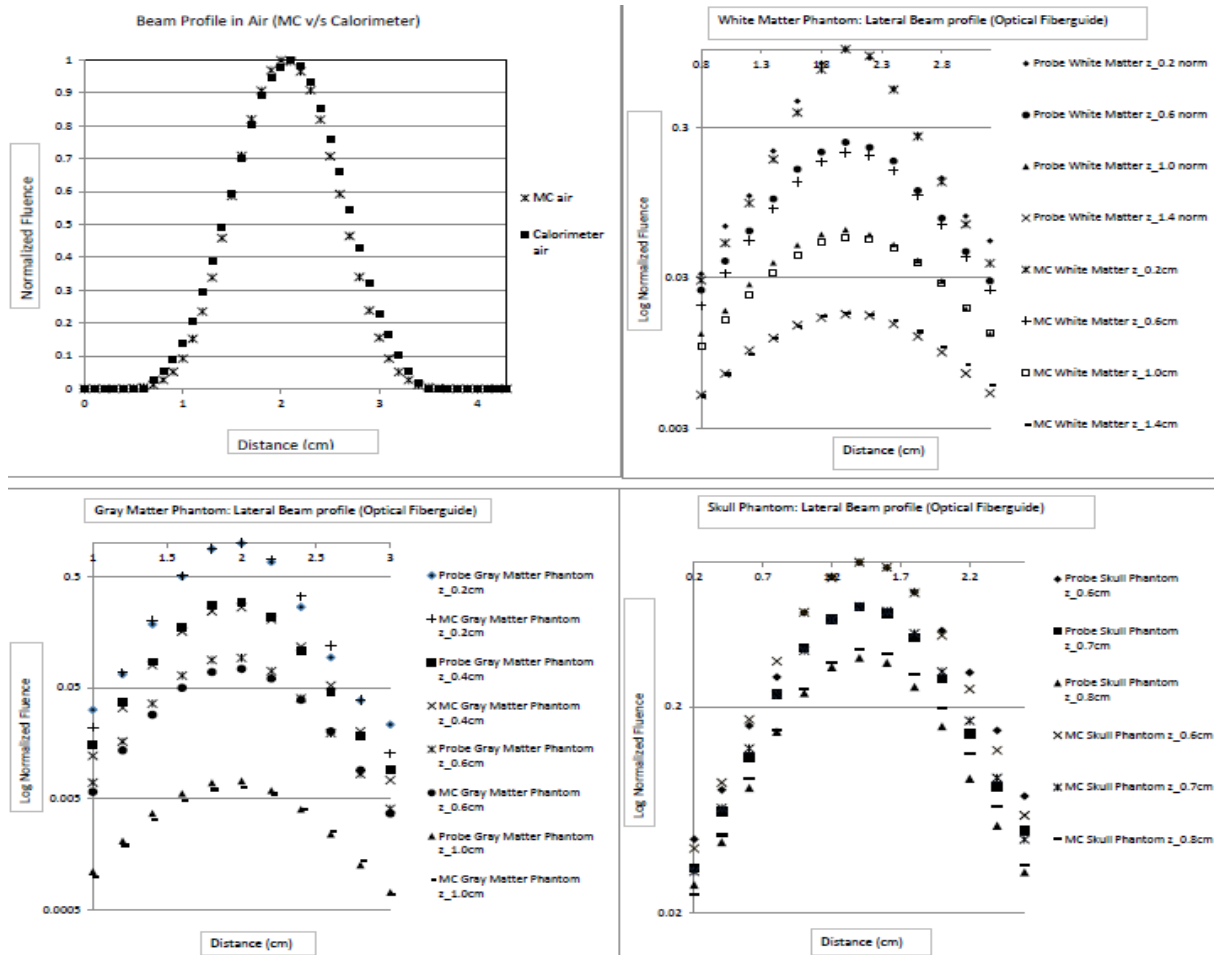


Figure 3. Plotted are the relative photon fluence as measured by the ODP and as simulated by the MC code for a super Gaussian laser beam in air (*top left*), white matter (*top-right*), gray matter (*bottom-left*), and skull (*bottom-right*).

iv. Sheep Skull and Brain Phantom: In combination with the phantom study from the previous section, an estimate of the attenuation of near infrared irradiation by the skull and brain tissue phantom was made. The laser beam emanating from the optical fiber bundle was measured in air using the ODP and used to determine the beam profile, e.g., super Gaussian function, and laser fluence. This laser beam was positioned as close to normal to the goat skull as possible. The thickness of the bone where the laser beam was exposed was measured to be 1.1cm using calipers and validated by CT scans. To measure the laser beam profile at the inner surface of the skull, the dosimetry probe was axially positioned within 4 mm of this inner surface, and using a 3-D micrometer, the ODP was translated perpendicular to the laser beam to measure the fluence profile and along the axis of the beam profile to determine the peak beam intensity as a function of the distance from the inner surface (see Figure 4). After applying the calibration factors (Section: Calibration of ODP), **the percent of the laser fluence transmitted through the skull was measured to 4.41% (SA2.A).** MC simulated data were consistent with these ODP measurements (see Figure 4).

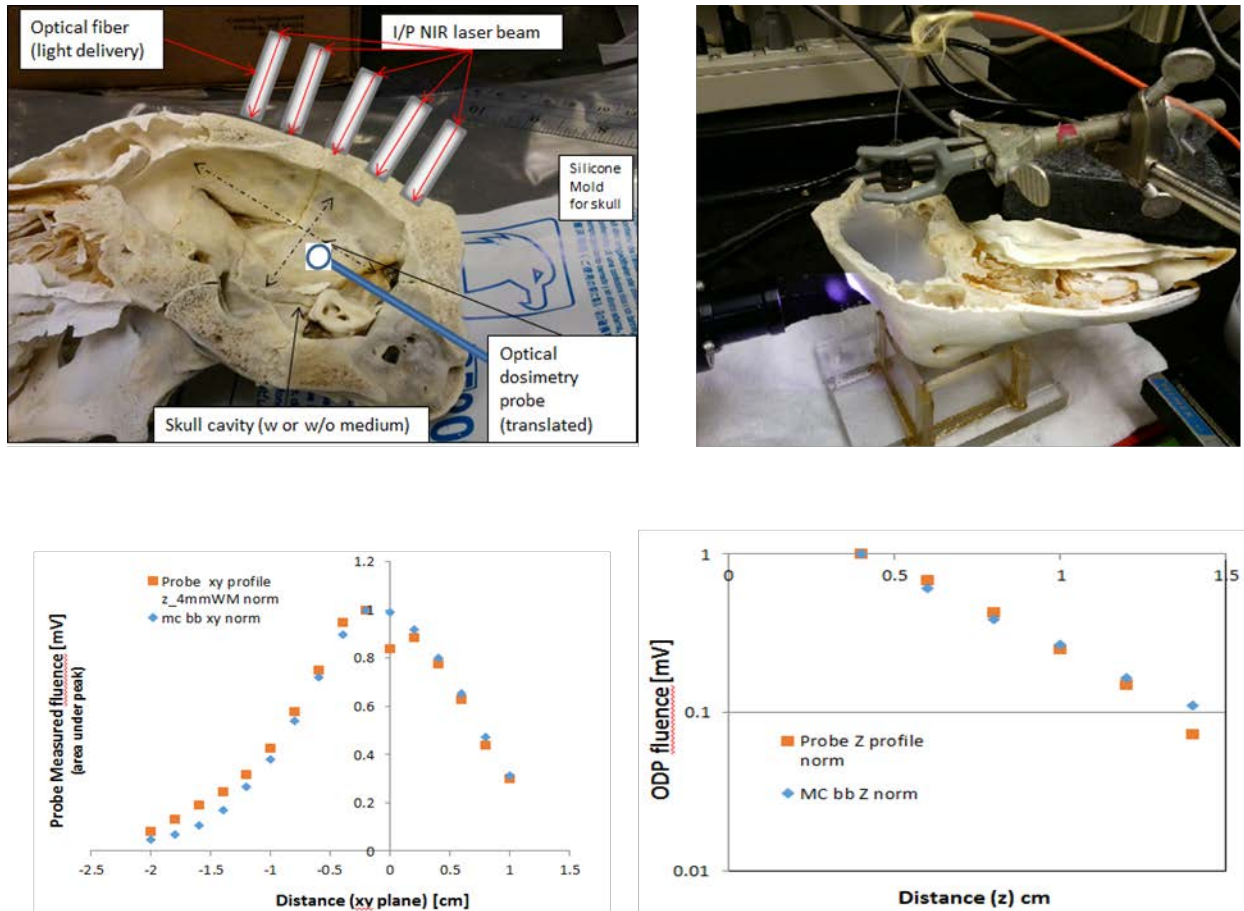


Figure 4. (Top row) Displayed are the photos of the goat skull and the ODP used in the phantom experiments. The picture on the right has the laser beam exposing the frontal bone (left to right) and the ODP embedded in the brain tissue phantom. **(Bottom row)** Plotted are the lateral profile near the inner surface of the skull and the axial profile along the central axis of the laser beam as measured by the ODP probe and simulated using the MC code.

With this same setup, the skull cavity was filled with a 4% intralipid solution. The ODP was used to measure the attenuation of the beam (Figure 4.c): the transmitted fluence was measured to be 7.25% per cm, which is consistent with Figure 2. If a 7.5% of intralipid (white matter) was used, the measured transmitted fluence

was 3.1% per cm, and gray matter was measured to be 0.31% per cm (see Figure 2). To relate these measurements to a human patient, average values for the thickness of the cortical gray matter and skull bone is determined. Cortical gray matter thicknesses can range from 2.0 to 5.0 mm, averaging around 4.7-4.85 mm [9, 10]. Skull bone thickness can range from 5.0 to 11.0 mm in an adult human head, averaging around 7.8 mm [11]. **Based on the above measurements, the average fluence transmitted through 8.0 mm of the skull bone would be 10.3% and through 4.8mm of gray matter would be 9.1%, or 0.93% on average through both tissues. Therefore, a tumor 4.5cm deep within the brain would receive approximately 8.5×10^{-9} of the laser fluence (SA2.B).**

Depending on the location of the tumor, the positioning of the optical sources could take into account the heterogeneity of the skull and gray matter. Optimally, a region of the skull and gray matter that that is 5mm (24.3% transmitted) and 2.5mm (20.0% transmitted) thick would increase the fluence to 1.9×10^{-8} , an improvement of a factor of 4.4. This suggests that a multiple number of sources optimally positioned for treatment based on the patient's anatomy may be beneficial.

v. Empirical Model of Photon Transport [2,3]: An empirical method was developed to simulate photon transport in tissue based on the acquired medical images of an individual patient (CT and MRI) with sufficient accuracy and at accelerated rates for clinical use. This approach is based on the assumption that the photon fluence in a voxel within a particular layer (or slice of an image) is the weighted sum of the fluence from its neighboring voxels in the previous layer. These weights determine the fraction of photons within a photon packet that is transported from one voxel to its neighbors relative to its average (or weighted) direction of propagation. It depends not only on a voxel-based geometry of the image but the voxel size and optical properties of the medium. It has been shown to faithfully reproduce the local shadowing effects from high absorbers (e.g., blood vessels) and high contrast media (Gold nanoparticles), and general attenuation in homogeneous tissue types. To determine the weights, MC simulations were performed in known media, such as white matter, gray matter, skull bone, and an Astrocytoma (tumor). Using these fluence profiles, the weights were modified until the photon fluence distribution from the empirical model matched (minimum in Chisquare) MC simulated results for different voxel sizes. A comparison between the photon fluence within each individual tissue type and for a

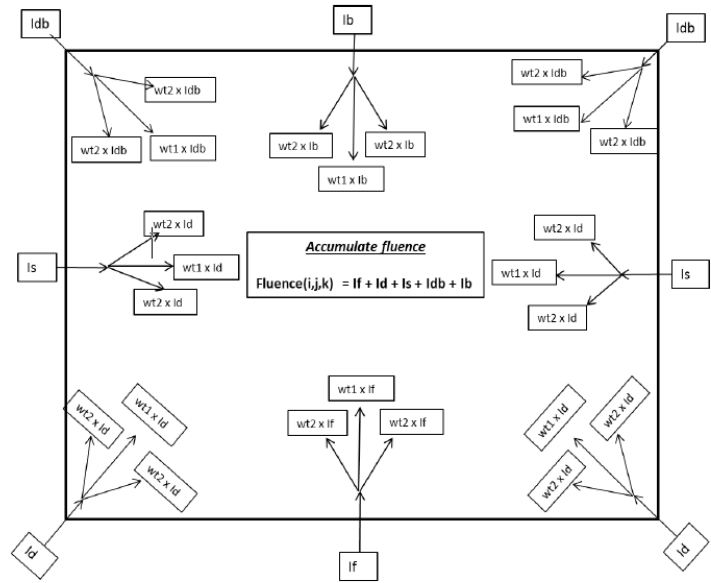


Figure 5. Displayed is a diagram depicting the local photon transport of the empirical model for a voxel within tissue. Note, this takes into account the general direction of the photon packet and the scattering properties of the tissue.

software phantom of the skull and brain are shown in Figure 6. There remains a relative small systematic effect (over estimate) of the photon fluence which requires further investigation, but the agreement is very good to develop and optimize delivery systems based on an individual patient's anatomy. When implemented on CUDA, the time it takes to simulate a human head with a broad beam source (e.g., super Gaussian beam) was on the order of seconds to low minutes where the MC would run in excess of 24 hours.

Future. We are currently applying our methods to mouse and dog models, and human scans. Multiple sources (lasers, semiconductor arrays) coupled with interventional methods are being investigated to improve NIR delivery to the brain. However, other methods will also be explored, such as radiation sensitive films to release these drugs.

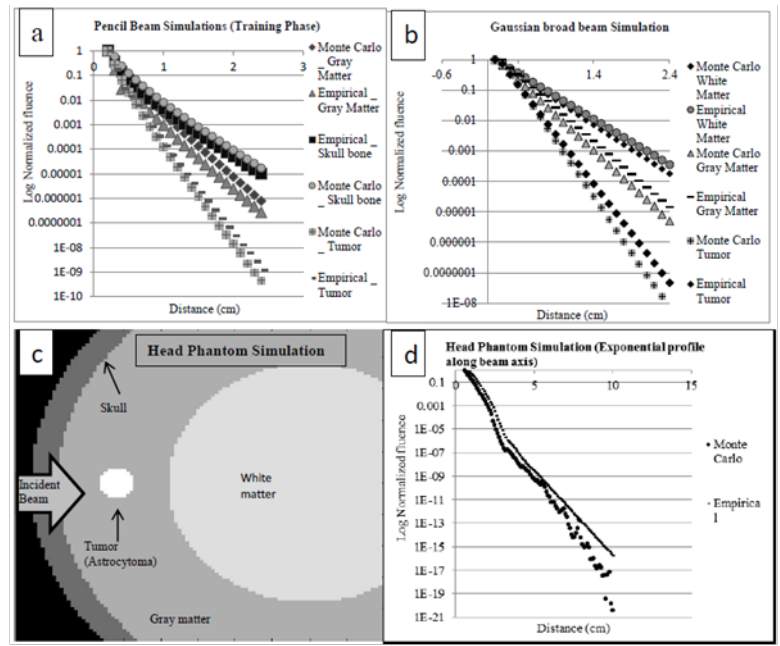


Figure 6. Comparison of the Empirical algorithm with MC simulations in homogenous (a,b) and heterogeneous (c,d) phantoms that resemble white matter, gray matter and astrocytoma. The plots in panels (a), (b), and (d) display the exponential decrease in fluence along the central axis of a Gaussian beam.

Tasks 1 d & e, 2c, and Task 3: These goals were unable to be met because of the issues with drug solubility (laptinib), light-triggered release, and probable leakage of doxorubicin from the NS@DNA@DOX nanocarriers. They all required the delivery of NS@DNA with stably loaded drug (DOX), which could be released by laser irradiation.

4. KEY RESEARCH ACCOMPLISHMENTS: *Bulleted list of key research accomplishments emanating from this research. Project milestones, such as simply completing proposed experiments, are not acceptable as key research accomplishments. Key research accomplishments are those that have contributed to the major goals and objectives and that have potential impact on the research field. If there is nothing to report, simply state "Nothing to report."*

- Nanocarriers

Earlier experiments by the Rice Nanophotonics Group suggest that DNA dehybridization and cargo release occurred by a non-thermal release mechanism involving hot-electrons [1]. The collective oscillation of surface conduction electrons in metallic nanoparticles induced by light at a resonant frequency is known as a localized surface plasmon. Upon excitation, surface plasmons can decay radiatively by re-emitting photons

of light or non-radiatively by the generation of local heat and/or energetic electrons. These energetic electrons are known as “hot-electrons” and the Rice group had hypothesized that the two DNA strands on the NS surface, which are negatively charged, were dehybridized by electrostatic interaction with the hot-electrons. It is now clear from the experiments conducted as a part of this research that at particle concentrations achievable within a tumor, dehybridization of the DNA double helix is a thermal phenomenon. This resolves a fundamental question as to how the NS@DNA nanocarriers function to release cargo. It has also led to the testing of the femtosecond pulsed laser as a work-around, which will enable sufficient heating at the nanoparticle surface to release cargo but insufficient bulk heating to cause protein denaturation and subsequent tissue damage.

- Delivery of infrared irradiation to brain

As pointed out earlier, prior to our work there was little data on the amount and distribution of near infrared light able to be delivered through the skull and brain tissue. We have been able to model this using both the sheep skull and phantom as well as the Monte Carlo simulations. This has led us to proposing that multiple simultaneous sources of IR irradiation with or without intracranial intervention methods is likely to be required to deliver a sufficient fluence of irradiation to effect drug release.

5. CONCLUSION: *Summarize the importance and/or implications with respect to medical and /or military significance of the completed research including distinctive contributions, innovations, or changes in practice or behavior that has come about as a result of the project. A brief description of future plans to accomplish the goals and objectives shall also be included.*

The delivery of effective therapeutics across the blood-brain barrier remains as critical a clinical challenge as it was when we first proposed our study. We remain convinced that the active delivery by macrophages of nanobound therapeutics to intracerebral malignancies is a promising strategy. Our studies have provided fundamental information on a number of aspects of the delivery of therapeutics by NS@DNA. 1. It is of key importance that the therapeutic is soluble and stable in aqueous solution; 2. Dehybridization of DNA duplexes on the nanoshell surface is a thermal phenomenon. 3. Although doxorubicin is a DNA intercalating agent, it may distort the double helix such that it is not a secure cargo. 4. We have estimated, to the best of our knowledge for the first time, the amount and distribution of near infrared light able to be delivered through the skull and brain tissue. While we have demonstrated substantial attenuation of the IR irradiation on its pathway through the skull and brain phantom, our results have prompted us to consider utilizing multiple NIR sources. Although this marks the end of our DoD funding, we hope to continue to pursue this novel delivery method. Should we secure future funding, we will determine if and to what extent DOX is leaking from the DNA duplex; presuming that DNA duplex distortion is responsible for the leakage, we will search for an alternate drug that can be maintained within the dsDNA@NS complex until release is triggered; and we will begin development of a new host (i.e. peptides)

for the DOX light triggered release process. With regard to delivering sufficient IR irradiation to the brain, the following are strategies that we hope to pursue:

- (1) Place multiple sources to avoid thicker regions of gray matter and overall skull density.
- (2) Increase the number of sources around the skull in order to get the fluence to plateau (instead of exponentially decay) at larger depths in the brain.
- (3) Examine the possibility of directional scattering in neuronal fibers as a means to increase NIR depth penetration.
- (4) Given the diffusive nature of light, it turns out that the beam surface area can be increased to reduce surface heating near the surface of the brain without too much loss in the fluence at depth.

We will also explore other methods such as radiation sensitive films from which to release drugs.

6. PUBLICATIONS, ABSTRACTS, AND PRESENTATIONS

a. List all manuscripts submitted for publication during the period covered by this report resulting from this project. Include those in the categories of lay press, peer-reviewed scientific journals, invited articles, and abstracts. Each entry shall include the author(s), article title, journal name, book title, editors(s), publisher, volume number, page number(s), date, DOI, PMID, and/or ISBN. Journal publications

1. Lay Press: Nothing to report

2. Peer-Reviewed Scientific Journals:

[1] Verleker AP, Fang Q, Choi M-R, Clare S, Stantz KM. An empirical approach to estimate near-infra-red photon propagation and optically induced drug release in brain tissues. Proc SPIE BiOS 9308-29: 1-8, 2015 (doi: 10.1117/12.2079991)

[2] Verleker AP, Fang Q, Choi M-R, Clare S, Stantz KM. An Optical Therapeutic Protocol to treat brain metastasis by mapping NIR activated drug release: a Pilot Study. Proc IEEE MIC (M19-96): 107, 2014.

[3] Verleker AP, Fang Q, Choi M-R, Clare S, Stantz KM. Dosimetric Validation of a Monte Carlo based Optical Planning Tool. *soon to be submitted to Applied Optics*

3. Invited Articles: Nothing to report

4. Abstracts: Nothing to report

b. List presentations made during the last year (international, national, local societies, military meetings, etc.). Use an asterisk () if presentation produced a manuscript.*

Nothing to report

7. INVENTIONS, PATENTS AND LICENCES

Nothing to report

8. REPORTABLE OUTCOMES:

Nothing to report

9. OTHER ACHIEVEMENTS: *This list may include degrees obtained that are supported by this award, development of cell lines, tissue or serum repositories, funding applied for based on work supported by this award, and employment or research opportunities applied for and/or received based on experience/training supported by this award.*

This project has directly contributed to the research thesis of Akshay Verleker at Purdue University, who will be graduating with a doctorate in 2016. It provided him the opportunity to submit and obtain a Purdue Research Foundation Grant (2014-2015), a Center for Cancer Research Travel Award (2014), and the Graduate Student Travel (Compton) Award from the College of Health and Human Sciences (HHS) (2015). These latter awards provided Akshay the opportunity to present this research at the IEEE Medical Imaging (NSS/MIC 2014) and SPIE BiOS (2015) conferences, where, at the former meeting, he was awarded the Nuclear and Plasma Sciences Society Phelps continuing education grant to pursue continuing education courses in the field of particle and photon transport and imaging sciences.

10. REFERENCES

- [1] Huschka R, Zuloaga J, Knight MW, Brown LV, Nordlander P, Halas NJ. Light-induced release of DNA from gold nanoparticles: nanoshells and nanorods. *J Am Chem Soc.* 2011 Aug 10;133(31):12247-55.
- [2] Huschka R, Neumann O, Barhoumi A, Halas NJ. Visualizing light-triggered release of molecules inside living cells. *Nano Lett.* 2010 Oct 13;10(10):4117-22
- [3] Verleker AP, Fang Q, Choi M-R, Clare S, Stantz KM. An empirical approach to estimate near-infra-red photon propagation and optically induced drug release in brain tissues. *Proc SPIE BiOS 9308-29:* 1-8, 2015 (doi: 10.1117/12.2079991)
- [4] Verleker AP, Fang Q, Choi M-R, Clare S, Stantz KM. An Optical Therapeutic Protocol to treat brain metastasis by mapping NIR activated drug release: a Pilot Study. *Proc IEEE MIC (M19-96):* 107, 2014.
- [5] Verleker AP, Fang Q, Choi M-R, Clare S, Stantz KM. Dosimetric Validation of a Monte Carlo based Optical Planning Tool. *soon to be submitted to Applied Optics*
- [6] Van der Zee, et al. Optical properties of brain tissue. *OE/LASE'93: Optics, Electro-Optics, and Laser Applications in science and Engineering.*
- [7] Firbank M, et al. Measurement of the optical properties of the skull in the wavelength range 650-950nm. *Phys. Med. Biol.* 38:503-510, 1993.
- [8] Fang Q et al. Monte Carlo simulation of photon migration in 3-D turbid media accelerated by graphics processing units. *Opt. express* 17:20178-20190, 2009.

- [9] Narr KL et al. Mapping Cortical Thickness and gray Matter Concentration in First Episode Schizophrenia. *Cerebral Cortex* 15:708-719, 2005.
- [10] AJilore O et al. Regional cortical gray matter thickness difference associated with type 2 diabetes and major depression. *Psychiatry Res* 184:63-70, 2010.
- [11] this is the skull bone thickness

11. APPENDICIES: *Attach all appendices that contain information that supplements, clarifies or supports the text. Examples include original copies of journal articles, reprints of manuscripts and abstracts, a curriculum vitae, patent applications, study questionnaires, and surveys, etc.*

- a. Manuscript: Proc SPIE BiOS 9308-29: 1-8, 2015
- b. Manuscript: Proc IEEE MIC (M19-96): 107, 2014.
- c. Draft manuscript: Verleker AP, Fang Q, Choi M-R, Clare S, Stantz KM. Dosimetric Validation of a Monte Carlo based Optical Planning Tool. *soon to be submitted to Applied Optics*

An Optical Therapeutic Protocol to treat brain metastasis by mapping NIR activated drug release: A Pilot Study

Akshay Prabhu Verleker, Qianqian Fang, Mi-Ran Choi, Susan Clare and Keith M. Stantz

Abstract—Treatment of Central Nervous System (CNS) metastasis poses a critical clinical challenge due to limitations in drug uptake across the blood brain barrier and blood-cerebrospinal fluid barrier. Recent research has shown the efficacy of using macrophages as drug carriers to target metastatic sites in the brain, which can then be activated by illuminating with near infrared radiation. The goal of this research is to develop an optically targeted therapeutic treatment of metastasis, specifically for metastatic breast cancer of the brain. As a first step towards accomplishing this, we developed a 3D Monte Carlo photon transport code capable of simulating phantoms with optical properties of brain and tumor; and validated the Monte Carlo simulated photon fluence within brain phantoms using an optical dosimetry probe. The phantom studies showed good correlation (correlation coefficient $R=0.977$) between the probe measurements and the Monte Carlo simulation in a white matter phantom (reduced scattering coefficient $\mu_s=8.25\text{mm}^{-1}$, absorption coefficient $\mu_a=0.005\text{mm}^{-1}$). Our future steps will be to implement the Monte Carlo to map out photon energy distribution in the brain, and subsequent drug release, by segmenting & translating head CT image volumes to corresponding optical properties of brain tissues. To access the therapeutic response, changes in the vascular physiology of the brain due to Her2 inhibition will be measured using dynamic contrast-enhanced imaging (e.g. DCE-CT), and with Monte Carlo based optical fluence maps. An optical treatment plan, using fast Monte Carlo software, optimized with CT segmented image volumes, would significantly reduce the treatment time and allow targeted drug activation while sparing healthy tissues.

I. INTRODUCTION

TREATMENT of Central Nervous System (CNS) metastasis poses a critical clinical challenge due to limitations in drug uptake in the brain (across the blood brain barrier and blood-cerebrospinal fluid barrier) and adverse neurotoxic effects of mainstay therapies such as whole brain radiation therapy (WBRT) and stereotactic radiosurgery.¹ With non-CNS metastasis being treated successfully with receptor targeted drug delivery, aided by improved imaging and localized radiotherapy techniques, the brain remains a sanctuary for

metastasis (e.g. triple negative and HER2+ breast cancer metastasis with median survival rates of 2 to 16 months).¹ This study is part of a project which demonstrated a macrophage based “Trojan Horse” delivery of fluorescent molecules into brain metastasis² and subsequent release of the fluorescent molecules on activation *in-vivo* by NIR radiation.³ The larger goal of this collaborative project is to deliver lapatinib-gold nanocomplex laden macrophages to brain metastasis and design a therapeutic protocol to optically stimulate drug release in target tissues in the brain. In the current project, the purpose is to design an optical simulation protocol (using Monte Carlo simulations) to effectively predict the photon distribution and subsequent drug activation in the brain tissue, and validate it by using an optical dosimetry probe. With the rate/quantity of drug release being directly dependent on the optical power delivered, the Monte Carlo simulation protocol, with the ability to predict photon distribution in heterogeneous brain tissue, can be used to generate an equivalent drug release map. The optical properties of the brain can be mapped by converting the CT image densities of the brain into the corresponding optical properties of the tissue (e.g. white/gray matter, CSF, etc.), which would serve as an input to the Monte Carlo routine. The optical drug release map generated by Monte Carlo can be co-registered with CT images to improve the therapeutic efficacy of the protocol.

In order to predict the photon energy distribution in heterogeneous brain tissue, we used a GPU based 3D Monte Carlo simulation code⁴, which was modified to generate user defined beam profiles to emulate the NIR (800 nm) laser source used in our lab. Monte Carlo simulation has been used as the gold standard for photon propagation studies (in 3D heterogeneous media), with the GPU version having acceleration speeds 100 to 300 times faster than corresponding CPU versions.⁴ In order to validate and quantify the Monte Carlo generated fluence in brain tissue phantoms, we used an optical dosimetry probe to measure the photon fluence in low optical fluence regions. An optimized treatment plan using a fast Monte Carlo software to predict *in vivo* drug release, would significantly reduce the treatment time and allow the targeted drug activation while sparing healthy tissues.

In addition to designing the Optical therapeutic protocol, we also looked into the feasibility of using Dynamic Contrast Enhanced CT (DCE-CT) imaging to monitor and quantify the efficacy of treatment. The vascular structure of a tumor is complex and heterogeneous, and is seen to vary between individual tumors and during different phases of tumor growth.⁵ This heterogeneity in tumor vasculature, characterized by hypoxia, anoxia and hypoglycemia, leads to differing response to treatment due to formation of barriers to transport and distribution of drug molecules.⁵⁻⁹ Following

Manuscript received Nov 14, 2014. This work was supported in part by the DoD/BCRP Grant (PI: Dr. Clare; Northwestern University), “Delivery of Nano-Tethered Therapies to Brain Metastases of Primary Breast Cancer Using a Cellular Trojan Horse”.

Akshay Prabhu Verleker is with the School of Health Sciences, Purdue University, West Lafayette, IN 47907 USA (email: aprabhuv@purdue.edu)

Qianqian Fang is with the Martinos Center for Biomedical Imaging, Massachusetts General Hospital, Harvard Medical School, Charleston, MA 02129 USA (email: fangq@nmr.mgh.harvard.edu)

Mi-Ran Choi is with the Feinberg School of Medicine Northwestern University, Chicago, IL 60611 USA (email: mi.choi@northwestern.edu)

Susan Clare is with the Feinberg School of Medicine Northwestern University, Chicago, IL 60611 USA (email: susan.clare@northwestern.edu)

Keith M. Stantz is with the School of Health Sciences, Purdue University, West Lafayette, IN 47907 USA (email: kstantz@purdue.edu)

treatment with anti-angiogenic or cytotoxic drugs, the tumor vasculature undergoes complex physiological and biological changes some of which are adaptive in nature.⁵⁻⁹ DCE-CT has been successfully used to simultaneously quantify physiological parameters such as perfusion and vascular plasma volume in tumors after treatment with therapeutic drugs.¹⁰⁻¹² Past research has proved the feasibility of using DCE-CT in measuring the physiological response of breast tumors to anti-angiogenic therapies using the two-compartmental model.¹¹⁻¹² In the present study we used the above model to obtain parametric maps of perfusion, permeability, fractional plasma volume and fractional interstitial volume in glioma tumors grown in mice; thus demonstrating the feasibility of DCE-CT imaging to monitor brain tumor response to treatment.

II. METHODS

Step 1: The optical dosimetry probe (1.5mm diameter) was calibrated using a calorimeter (Gold standard) in low fluence regions. The probe measurements were used to validate Monte Carlo generated photon fluence in brain phantoms resembling white and gray matter, made with specific concentrations of India ink (absorber) and Intralipid (scatterer),¹³⁻¹⁴ as measured by photo-spectrometer (Gold standard), consistent with brain tissue and tumors (values) as shown in Fig 1. The source of light used was an integrating sphere connected to a pulsed NIR laser with wavelength 800 nm, frequency 200MHz, and energy 10mJ/pulse. The broad beam NIR output power emanating from the integrating sphere was 0.2083mW/mm².

Step 2: In order to apply the Monte Carlo (MC) simulation protocol to the brain, we designed a segmentation software to determine tissue boundaries in the brain using Computed tomography images. The CT image densities in Hounsfield units (HU) of the brain were translated into corresponding optical properties (absorption coefficient, scattering coefficient, and anisotropy factor) using lookup tables (Fig 2). The lookup tables were prepared from earlier studies which derived the Hounsfield units and optical properties of brain tissues such as white/gray matter.¹³⁻¹⁵ The segmentation software generated an optical map of the brain, which was given as input to the Monte Carlo. The photon energy map generated by the Monte Carlo can be co-registered with the CT image to visualize the efficacy of drug release.

Step 3: "Optical treatment protocol", voxel-based optical properties of a human head (obtained from CT scans) were input into MC code to simulate 3D fluence maps from multiple (optically coupled) light sources. This study also looked into the feasibility of monitoring effectiveness of targeted drug release by monitoring the physiology at target sites and surrounding tissues. An Orthotopic model of glioblastoma tumors were grown in mice and parametric images of perfusion, permeability, fractional plasma volume and fractional interstitial volume were derived using the two compartmental model.¹²

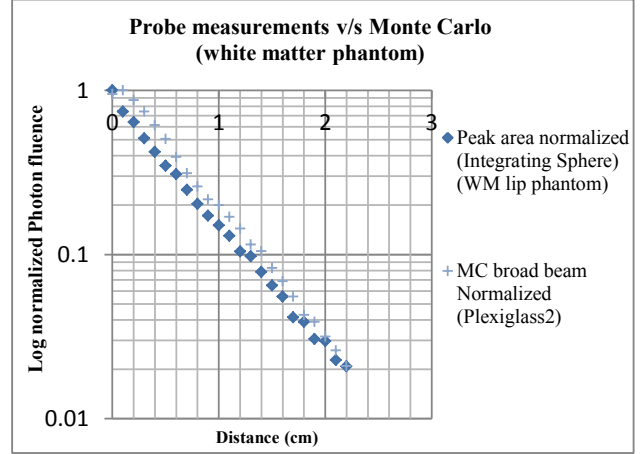


Fig. 1. Validation of Monte Carlo simulated photon fluence (1/mm²) with probe measurements (peak area in mV) in a white matter phantom. Log normalized fluence plotted v/s depth in a white matter phantom. Correlation R=1.

III. OBSERVATIONS & RESULTS

The Monte Carlo generated photon fluence was validated by probe measurements in optical brain phantoms (e.g. white matter in Figure 1). The optical fluence measured by the probe was in turn, calibrated using a calorimeter (Gold standard) and showed a linear and isotropic response to input NIR fluence at different incidence angles (<5% variation). Our MC simulation studies showed that 99% of photons are attenuated by the bone (1cm), which was confirmed by probe measurements in an empty goat skull. The segmentation code (with iterative Monte Carlo) can be used to identify regions of least bone thickness and determine the path of least attenuation to couple maximum power to brain tissues. This study proved that an optimized Monte Carlo could be successfully used to quantify photon propagation in the brain and thus predict the rate of drug release in target tissues to depths up to 5cm in brain tissues.

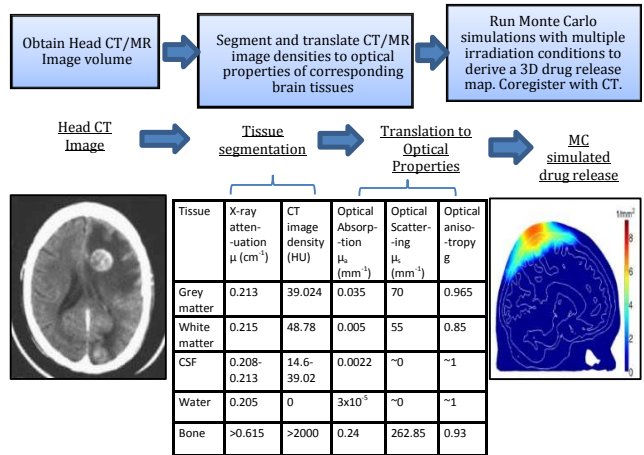


Fig. 2. Monte Carlo based treatment protocol. Head CT image densities (in Hounsfield Units/HU) are segmented and translated into optical properties of the brain tissue (white/gray matter, CSF, skull bone, etc.). Monte Carlo routine is then used to simulate light propagation through the brain. [CT image reference: <http://www.mpoullis.com/thored/rad/23.htm>]¹⁶

Our preliminary longitudinal study has indicated that DCE-CT is an effective tool to study tumor progression and physiology (Fig 3) of glioma tumors. We propose to monitor these effects by studying the change in fractional plasma volume and fractional interstitial volume, both of which are excellent indicators of vascular physiology (Fig 3).

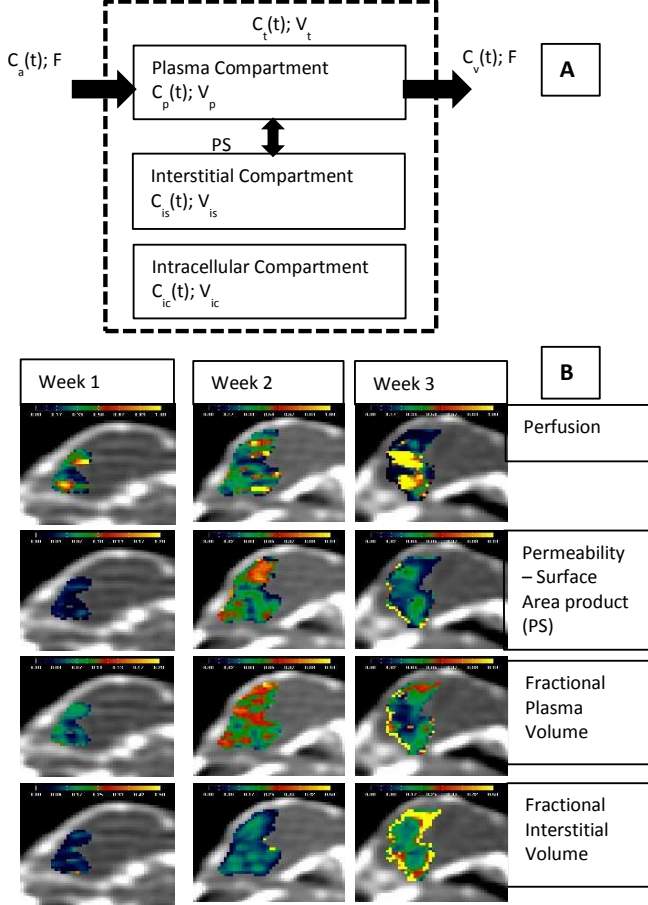


Fig. 3. Monitoring cancer therapy through Dynamic Contrast Enhanced CT (DCE-CT). (A) Schematic of two compartmental model.¹² (B) Parametric images of glioblastoma (orthotopic model) grown in mice. In this longitudinal study, parametric images were obtained of perfusion, permeability, fractional plasma volume and fractional interstitial volume of glioma tumors grown in mice using the two compartmental model. These parameters can be used to quantify the efficacy of treatment, thus proving effectiveness of using DCE-CT to monitor targeted drug therapy.

IV. DISCUSSION

In this study, we have assumed that the quantity of drug release is proportional to the optical power coupled to the tissues (as shown in previous *in-vitro* studies). Future studies will focus on quantifying the optical drug release threshold by determining the relationship between optical power coupled and amount of drug released. Further studies will involve adjusting beam profiles to optimize the coupling and localization of optical energy in the brain for maximal drug release. In order to monitor tumor response to therapy, DCE-CT will be used to further study vascular normalization¹⁷ in tumors caused by anti-angiogenic effects of lapatinib drug, which can help in optimizing therapeutic efficacy.

V. CONCLUSION

This study has successfully demonstrated the potential of using a fast voxel based Monte Carlo based routine to predict the rate of drug release in heterogeneous brain tissue by using Computed Tomography images to segment and translate tissue boundaries of the brain. An optimized therapeutic protocol with a fast Monte Carlo routine can be used to determine the best irradiation conditions for targeted drug release in brain tissue within clinically relevant time frames.

VI. ACKNOWLEDGEMENT

We would like to thank Justin Sick and Fahed Alsanea for their contribution in developing experimental setups and Michael Shaffer for his work in developing the optical dosimetry probe. We are grateful to our collaborators Naomi Halas, Amanda Goodman and Sandra Bishnoi for their contributions in developing the drug nanocomplexes for optically activated drug release.

REFERENCES

- [1] A Niwinska, et al., "Breast cancer brain metastases: differences in survival depending on biological subtype", *Ann Oncol*, 2010, 21: 942–948.
- [2] Mi-Ran Choi, et al., "Delivery of nanoparticles to brain metastases of breast cancer using a cellular Trojan horse", *Cancer Nano*, 2012; 3: 47–54.
- [3] Mi-Ran Choi, et al., "A cellular Trojan Horse for delivery of therapeutic nanoparticles into tumors", *Nano Lett*, 2007; 7(12):3759–3765.
- [4] Q. Fang, et al., "Monte Carlo simulation of photon migration in 3D turbid media accelerated by graphics processing units", *Opt. Express* 2009; vol. 17.
- [5] P. W. Vaupel, "The influence of tumor blood flow and microenvironmental factors on the efficacy of radiation, drugs and localized hyperthermia", *Klin Padiatr.*, vol. 209, 1997, 243–249.
- [6] K. D. Miller, "Issues and challenges for antiangiogenic therapies," *Breast Cancer Res. Treat.*, vol. 75, no. Suppl 1, 2002, S45–S50.
- [7] B. S. Kuszky, F. M. Corl, F. N. Franano, D. A. Bluemke, L. V. Hofmann, B. J. Fortman, and E. K. Fishman, "Tumor transport physiology: Implications for imaging and imaging-guided therapy," *AJR Am. J. Roentgenol.*, vol. 177, 2001, 747–753.
- [8] Bergers G, Hanahan D, "Models of resistance to anti-angiogenic therapy." *Nat Rev*, 2008, 8:1592Y1603.
- [9] Grepin R, Pages G, "Molecular mechanisms of resistance to tumor anti-angiogenic strategies," *J Oncol*, 2010, 1835680.
- [10] Kan Z, Phongkitkarun S, Kobayashi S, Tang Y, Ellis LM, Lee TY "Functional CT for quantifying tumor perfusion in antiangiogenic therapy in a rat model," *Radiology*, 2005, 237:1151Y1158.
- [11] Stantz, Keith M., et al. "Monitoring the longitudinal intra-tumor physiological impulse response to VEGFR2 blockade in breast tumors using DCE-CT." *Molecular Imaging and Biology*, vol. 13(6), 2011, 1183–1195.
- [12] Cao, Minsong, et al. "Developing DCE-CT to quantify intra-tumor heterogeneity in breast tumors with differing angiogenic phenotype." *Medical Imaging, IEEE Transactions on*, vol. 28(6), 2009, 861–871.
- [13] Van der Zee et al., "Optical properties of brain tissues", *OE/LASE'93: Optics, Electro-Optics, and Laser Applications in Science and Engineering*, International Society for Optics and Photonics, 1993.
- [14] Wai-Funf Cheong et al., "A review of the Optical Properties of Biological Tissues", *IEEE journal of quantum electronics*, 1990, 2166–2185.
- [15] Arimitsu Tetsuo et al., "White-Gray Matter Differentiation in Computed Tomography", *Jou rnal of Computer Assisted Tomography*, 1977, 437
- [16] Mike Poullis, "Lung Cancer, Staging," [online], <http://www.mpoullis.com/thorcd/rad/23.htm> (Accessed: 3 November 2014).
- [17] Jain, Rakesh K. "Normalization of tumor vasculature: an emerging concept in antiangiogenic therapy," *Science*, 2005, 307.5706, 58–62.

An empirical approach to estimate near-infra-red photon propagation and optically induced drug release in brain tissues

Akshay Prabhu Verleker^{*a}, Qianqian Fang^b, Mi-Ran Choi^c, Susan Clare^c and Keith M. Stantz^a

^aDepartment of Health Sciences, HAMP 1263, 550 Stadium Mall Drive, West Lafayette, IN, USA

47907-2051; ^bMartinos Ctr. for Biomedical Imaging, Harvard Medical School, Charleston, MA

USA, ^cFeinberg School of Medicine, Northwestern University, Chicago, IL.

ABSTRACT

Purpose: The purpose of this study is to develop an alternate empirical approach to estimate near-infra-red (NIR) photon propagation and quantify optically induced drug release in brain metastasis, without relying on computationally expensive Monte Carlo techniques (gold standard). Targeted drug delivery with optically induced drug release is a non-invasive means to treat cancers and metastasis. This study is part of a larger project to treat brain metastasis by delivering lapatinib-drug-nanocomplexes and activating NIR-induced drug release. The empirical model was developed using a weighted approach to estimate photon scattering in tissues and calibrated using a GPU based 3D Monte Carlo. The empirical model was developed and tested against Monte Carlo in optical brain phantoms for pencil beams (width 1mm) and broad beams (width 10mm). The empirical algorithm was tested against the Monte Carlo for different albedos along with diffusion equation and in simulated brain phantoms resembling white-matter ($\mu_s'=8.25\text{mm}^{-1}$, $\mu_a=0.005\text{mm}^{-1}$) and gray-matter ($\mu_s'=2.45\text{mm}^{-1}$, $\mu_a=0.035\text{mm}^{-1}$) at wavelength 800nm. The goodness of fit between the two models was determined using coefficient of determination (R-squared analysis). Preliminary results show the Empirical algorithm matches Monte Carlo simulated fluence over a wide range of albedo (0.7 to 0.99), while the diffusion equation fails for lower albedo. The photon fluence generated by empirical code matched the Monte Carlo in homogeneous phantoms ($R^2=0.99$). While GPU based Monte Carlo achieved 300X acceleration compared to earlier CPU based models, the empirical code is 700X faster than the Monte Carlo for a typical super-Gaussian laser beam.

Keywords: Empirical algorithm for light propagation, NIR photon propagation, Monte Carlo simulation, Optical therapy, Optically induced drug release, Tissue Optics, Light Scattering

1. INTRODUCTION

Optical therapy using NIR light delivery requires the estimation of photon fluence in tissues and heterogeneous media. This study is a part of a larger project which seeks to selectively deliver macrophages laden with lapatinib-gold-nanocomplex drug molecules to brain metastasis with over-expressed HER2+ receptors and activate targeted drug release using NIR photons.^{1,2} The effectiveness of achieving a targeted drug delivery and optically activated drug release with a Monte Carlo based optical therapeutic protocol has been demonstrated in previous studies.¹⁻⁵ The design of an optical therapeutic protocol requires the evaluation of various illumination conditions such as the angles of incidence and source positions for optimum drug release in the metastatic lesions of the brain.⁵ While the Monte Carlo is the gold standard for photon estimation in 3D media, it is computationally expensive to be used over a large number of iterations. Hence there is a need for a computationally efficient evaluation algorithm which can reduce the possible illumination conditions to a few iterations, while minimizing error in fluence estimation. This algorithm should also be able to interface seamlessly with any imaging modality system to effectively localize fluence distributions with respect to anatomical and physiological information provided by imaging modalities such as CT, Ultrasound, PET, MRI, etc. In the current work we have developed a fast voxel based empirical approach which can estimate photon fluence in the brain and evaluate different illuminations before using Monte Carlo as a final tool for validation. Being a 3D voxel based method; this algorithm can be easily integrated with other imaging modalities to evaluate fluence distributions in the brain and other tissues, by co-registering 3D fluence images with images from CT, MR, Ultrasound, etc.

Light propagation studies in 3D media rely on the use of Monte Carlo simulations as the gold standard, to estimate the photon fluence distribution in three dimensional units of volume known as voxels. The Monte Carlo model uses probability distribution to generate a random walk of photons in three dimensional media and relies on generating a large number of events to produce statistically significant fluence distributions in optical media with specific absorption and

scattering properties.⁶⁻¹⁰ The photon fluence deposited (and traversing) within each voxel depends on the specified optical properties assigned by the user, such as the absorption coefficient (μ_a), scattering coefficient (μ_s), anisotropy factor (g) and refractive index (n). The traditional Monte Carlo software is computationally expensive as it relies on generating millions of photons and tracking each photon as it propagates through the medium. Recent research in GPU based Monte Carlo by the Fang group has resulted in speeds up to 300X faster than the traditional CPU based versions.⁶ However for large optical datasets, such as those obtained and translated from CT or MR images, and under wide beam illumination conditions, the Monte Carlo suffers from slow computation speeds due to large photon propagation times in highly scattering tissues. This results in a drawback and slowdown in the process of planning targeted light delivery to specific regions within the human body. In this study we have designed an alternate empirical approach to light propagation which can estimate the photon fluence in tissues in complex three dimensional media to provide a fast preliminary approach to light estimation while planning targeted NIR light delivery. The purpose of this study is to devise a fast means to estimate NIR photon fluence under different illumination conditions in an optical treatment plan before using Monte Carlo for final verification and corrections.

The empirical approach estimates the fluence distribution in a voxelated medium by using a weighted approach to fluence propagation from one layer to the next. The assumption used is that the photon fluence in a voxel is a weighted sum of the fluences in the neighboring voxels of the preceding layer. The weights are arbitrarily assigned to each voxel based on its optical properties, mainly the scattering coefficient. The accuracy of the empirical approach depends on the optimization method used to estimate the weights for each set of optical properties. The empirical approach simulates photon scatter by dividing the fluence into scattering vectors in the forward and diagonal directions, while photon absorption is simulated using the Beer Lambert's rule.¹¹ An optimization routine is used to estimate the weights assigned to each voxel by comparing with a pencil beam simulated by the Monte Carlo. In this study we estimated the weights for typical brain tissues such as Gray Matter, White Matter, Skull bone and Astrocytoma with known optical properties.¹²⁻¹⁴ These weights were then tested in homogeneous and heterogeneous brain phantoms under pencil beam and broad beam illumination. The Monte Carlo has been used as the gold standard for evaluating the performance of this algorithm. The 3D GPU based Monte Carlo, developed by the Fang group, has an acceleration of 300X over the traditional CPU based version⁶, while the Empirical approach was seen to be 700X faster than the GPU based Monte Carlo for a super-Gaussian beam.

2. MATERIALS AND METHODS

2.1 Algorithm Design

The empirical approach approximates the photon scatter from one voxel to the next by assigning weights to the scattering directions. The main goal of this algorithm is to approximate the total scattering events within a voxel into 14 component vectors. Since tissues are mostly forward propagating with anisotropies approximately equal to or greater than 0.9, it can be assumed that most photon scatter directions can be approximated into forward and diagonal vectors. Hence, each scattering event is divided into 4 scattering components: one forward component with the wt1 and 4 diagonal components with weight wt2 as shown in the figures. The fluence enters a voxel from 14 neighboring voxels. Each incoming fluence component is then scattered into one forward component and 4 diagonal components. The total fluence in each individual direction is accumulated and absorbed within a voxel based on the absorption coefficient. The remaining fluence then exits the voxel into the 14 neighboring voxels. It is important to note that the fluence entering a voxel is equal to the sum of fluence absorbed within the voxel and the fluence exiting the voxel. This is achieved by ensuring that the sum of the weights used is equal to one [i.e. $(wt1 + 4 \times wt2) = 1$].

The steps of the algorithm can be summarized as follows:

- 1) Assign the incident photon fluence (e.g. Gaussian beam) to the first layer of voxels. Here we have assumed that the photons enter the volume (of dimensions $dim1 \times dim2 \times dim3$) at $z=1$ (first layer).
- 2) Begin the propagation from layer $z=1$ to $z=dim3$.

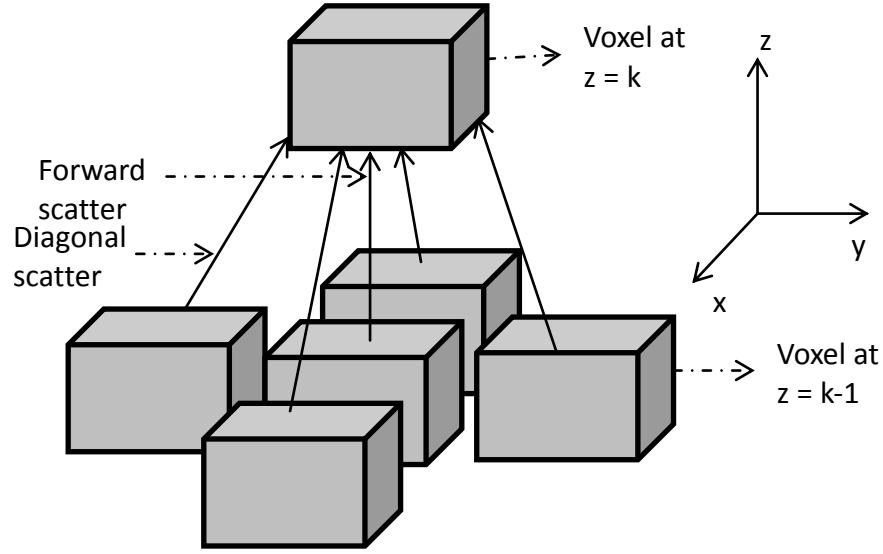


Figure 1: Step1: Modelling photon propagation. The empirical algorithm propagates photons from one layer to the next by assigning weights to fluences in voxels of the preceding layer. The figure shows forward and diagonal scatter from layer $k-1$ to k .

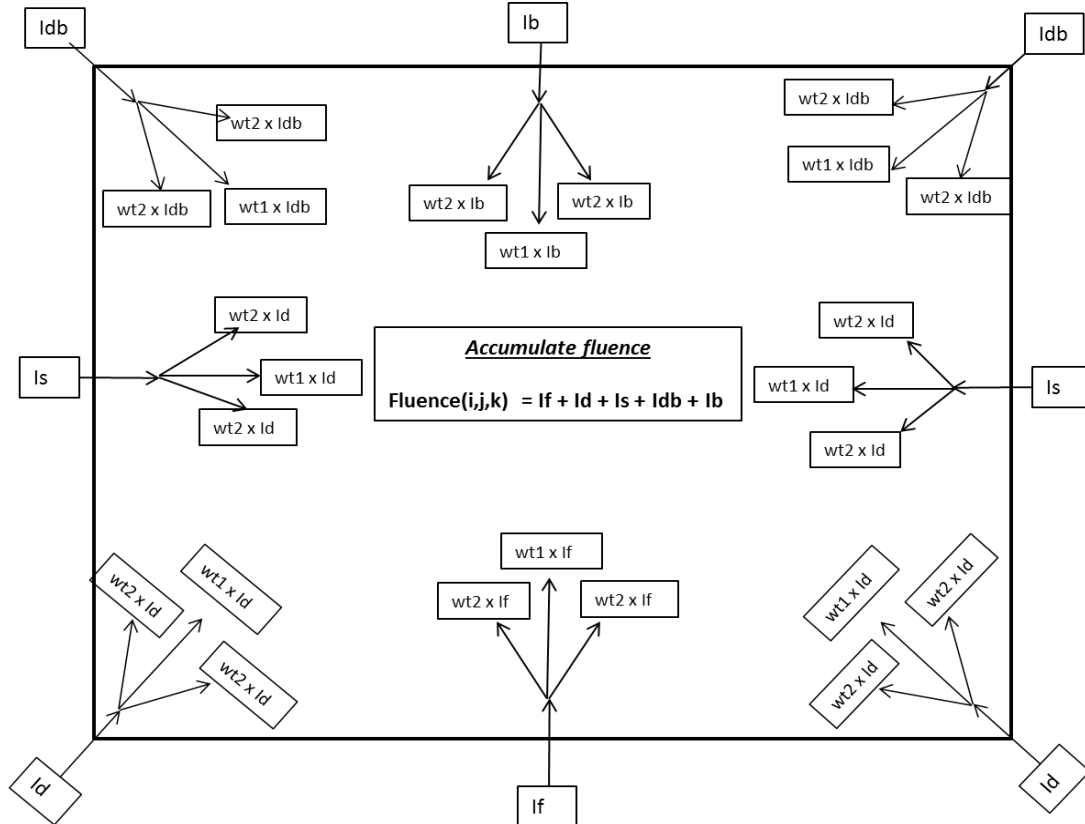


Figure2: Step2: Fluence Accumulation within a voxel. The figure shows the accumulation of directional photon fluences from neighboring voxels, namely the forward (If), diagonal upwards (Id), diagonal downwards (Idb) and side (Is) scattered component fluences. The fluence entering a voxel is scattered into 5 directions: 4 diagonal directions with the weight $wt2$ and one forward direction with the forward weight $wt1$. The weights are chosen such $(wt1 + 4 \times wt2) = 1$.

3) For every voxel in a layer $z=k$:

- a) Calculate the 14 directional components from the incident photon fluence. For the first layer the fluence is assumed to be in the forward direction. The fluence from neighboring voxels is accumulated in each direction as follows:

$$\text{Forward Component} = I_f(x,y,z) = \sum (\text{forward components} \times \text{wt1}) + \sum (\text{forward diagonal components} \times \text{wt2})$$

$$\text{Forward Diagonal Component} = I_d(x,y,z) = \sum (\text{forward components} \times \text{wt2}) + \sum (\text{forward diagonal components} \times \text{wt1}) + \sum (\text{side components} \times \text{wt2})$$

$$\text{Side Component} = I_s(x,y,z) = \sum (\text{forward diagonal components} \times \text{wt2}) + \sum (\text{side components} \times \text{wt1}) + \sum (\text{backward diagonal components} \times \text{wt2})$$

$$\text{Backward Diagonal Component} = I_{db}(x,y,z) = \sum (\text{side components} \times \text{wt2}) + \sum (\text{backward diagonal components} \times \text{wt1}) + \sum (\text{backward component} \times \text{wt2})$$

$$\text{Backward Component} = I_b(x,y,z) = \sum (\text{backward component} \times \text{wt1}) + \sum (\text{backward diagonal components} \times \text{wt2})$$

$$\text{Total Fluence} = I(x,y,z) = I_f(x,y,z) + \sum I_d(x,y,z) + \sum I_s(x,y,z) + \sum I_{db}(x,y,z) + I_b(x,y,z)$$

The forward component (I_f) refer to the direction of propagation of the main fluence beam (or ‘forward scatter’), while the backward component (I_b) refers to the 180 degree scatter (or backscatter) which is opposite to the incident photon fluence vector. The diagonal components are divided into 4 forward diagonals (I_d) and 4 backward diagonals (I_{db}). Thus each direction is associated with a neighboring voxel. The total fluence within a voxel is obtained by summing up the fluences in each component directions. Note that the above directions can be arbitrarily chosen according to the experimental setup or at the convenience of the user.

- b) Simulate photon absorption by depositing the photon fluence into the voxel based on its absorption coefficient (μ_a):
 $\text{Absorbed Fluence} = I_{abs}(x,y,z) = I(x,y,z) \times \{1 - \exp(-\mu_a \times dl)\}$
 (where dl = path length)

4) Once fluences have been accumulated over the current layer, increment z to proceed to the next layer. Thus by repeating this process for all layers and updating the directional components of fluences for every voxel, the empirical approach propagates the fluence from one layer to the next across the volume.

2.2 Optimization Phase (Pencil beam simulations)

Optical properties of the medium (scattering coefficient μ_s , anisotropy factor g , absorption coefficient μ_a , albedo a') define the photon fluence generated by the empirical approach. The weights assigned to each voxel depend on its scattering property, while the absorption coefficient determines the amount of fluence deposited and energy absorbed. The weights were derived during the optimization phase by comparing the exponential attenuation profiles of the Empirical approach to the Monte Carlo using root mean square error and coefficient of correlation criteria. Previous studies have shown the applications as well as the limitations of the diffusion equation in estimating photon fluence for media with low albedos.^{10,15-22} In this study we first tested the performance of the Empirical approach with respect to the Monte Carlo and the diffusion equation for media with different albedos from 0.7 to 0.99. The albedo (a')¹⁰ is given by the equation:

$$a' = \frac{(1 - g)\mu_s}{(1 - g)\mu_s + \mu_a} \quad (1)$$

Next, the empirical algorithm was trained to derive the forward ($wt1$) and diagonal ($wt2$) weights for brain tissues such as white matter ($\mu_a=0.005\text{mm}^{-1}$, $\mu_s=55\text{mm}^{-1}$, $g=0.85$, $a'=0.9994$), gray matter ($\mu_a=0.035\text{mm}^{-1}$, $\mu_s=70\text{mm}^{-1}$, $g=0.965$, $a'=0.9859$), skull bone ($\mu_a=0.024\text{mm}^{-1}$, $\mu_s=18.4\text{mm}^{-1}$, $g=0.9$, $a'=0.9871$) and tumor (astrocytoma) ($\mu_a=0.3\text{mm}^{-1}$, $\mu_s=500\text{mm}^{-1}$, $g=0.88$, $a'=0.995$).¹²⁻¹⁴ A pencil beam was simulated using the Monte Carlo using the known optical

properties of each of the above brain tissues.¹²⁻¹⁴ The Empirical algorithm was then trained to emulate the same exponential decay profile by incrementing the forward scattering weight from 0 to 1, while the diagonal was adjusted to ensure that $wt1 + (4 \times wt2) = 1$. The weights derived from the optimization phase were used for the broad beam simulations in homogeneous and heterogeneous phantoms.

2.3 Broad beam simulations in Homogeneous and Heterogeneous Brain phantoms

The empirical weights obtained from the pencil beam training phase were used for further simulations using broad beams in homogeneous and heterogeneous brain phantoms. The Gaussian beam generated by the Monte Carlo was matched to that of the Empirical algorithm. An optical property map was generated in which every voxel was assigned a specific weight and absorption coefficient based on the tissue property. The Gaussian beam distribution was first tested in homogenous phantoms of each of the brain tissues: skull bone, gray matter, white matter and tumor (astrocytoma). The weights derived from the pencil beam optimization phase were used in the broad beam simulation to test their validity. Next, a software phantom of a human head with 15 cm diameter was created using concentric spheres to denote the different tissue types. The incident beam had a Gaussian profile. The fluence profiles and absorption energy maps generated Monte Carlo and Empirical approach were compared. The execution times for generation of a broad beam profile was compared between the two models.

3. RESULTS

3.1 Pencil beam simulations (Optimization Phase)

In this study, the empirical software was trained in an iterative process by comparing its exponential decay profiles to that of the Monte Carlo using pencil beams in optically homogeneous media. The Empirical approach had a better fit to the Monte Carlo as compared to the diffusion equation, especially for low albedos. The weights $wt1$ and $wt2$ were derived and optimized for each of the brain tissues (white matter, gray matter, skull bone and tumor) by using the profile which best matched the Monte Carlo. The absorption coefficient assigned was the same as has been obtained from previous studies. Figure 3 shows the pencil beam simulation profiles obtained by the Monte Carlo and the Empirical algorithm.

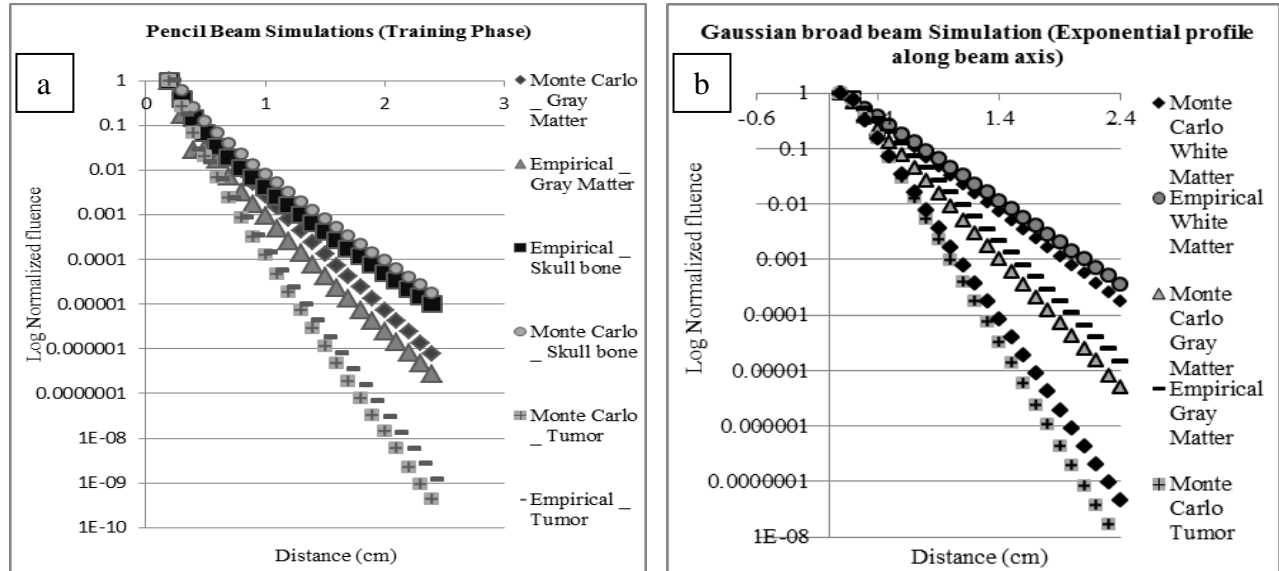


Figure 3. (a) Training Phase. The figure shows pencil beam profiles along z axis between the Monte Carlo and the Empirical algorithm. The empirical algorithm is trained to emulate the same exponential fluence attenuation as that of the Monte Carlo by adjusting and optimizing the weights $wt1$ and $wt2$. (b) Broad beam simulations: The empirical algorithm was compared to the Monte Carlo for incident Gaussian beam profiles. Overall the fluence profile of the Empirical closely followed that of the Monte Carlo.

The pencil beam simulations show that the empirical algorithm can be effectively trained to emulate the fluence attenuation for pencil beams generated using Monte Carlo in a homogeneous tissue medium. The pencil beams obtained by the empirical closely match the Monte Carlo with R-square value of 0.99. Since this study looks at the effectiveness of using the empirical approach to quantify optical drug release in the brain, we have obtained the weights mainly for brain tissues. These weights are then used to validate the fluence for broad beams such as Gaussian and super Gaussian beams.

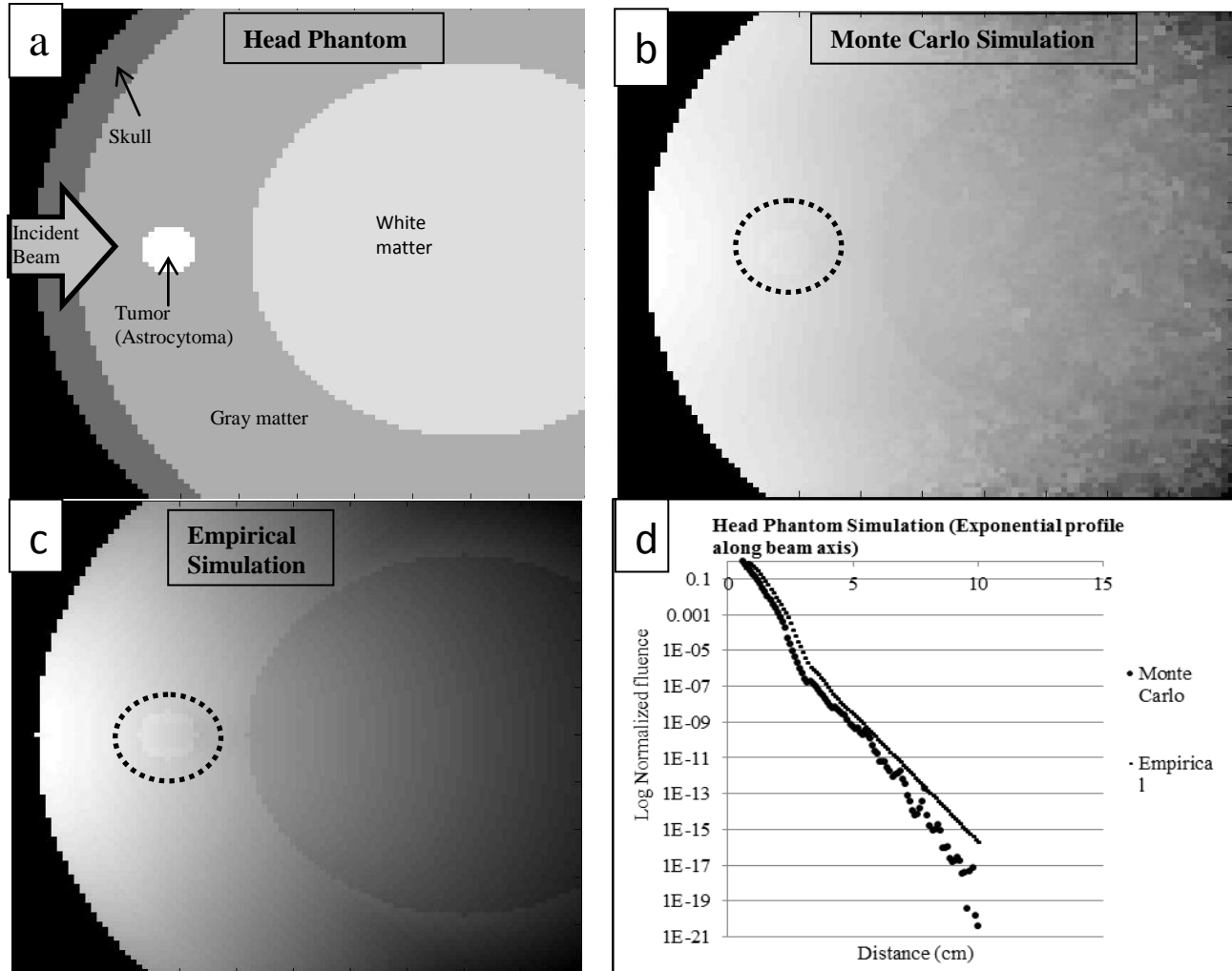


Figure 5: Validation in a Heterogeneous Head Phantom simulation. (a) Design of the head phantom. The image is obtained from the voxel properties/tissue types assigned in a 100 x 100 x 100 volume of 1mm voxel size. (b) Photon energy absorbed as obtained by the Monte Carlo simulation of a Gaussian beam traversing through the head phantom. (c) Empirical energy absorbed profile. (d) Photon fluence attenuation in along the incident beam axis at the beam center. The weights obtained from the training phase were assigned to the voxels in the empirical algorithm.

3.2 Broad beam simulations (Gaussian beam)

Figure 3(b) compares the Gaussian beam attenuation along beam axis between the Empirical and the Monte Carlo. The Gaussian beam analysis shows that the empirical approach can emulate the Monte Carlo fluence for broad beam simulations. The acceleration provided by the Empirical algorithm was approximately 700X as compared to the Monte Carlo for a broad beam. This however depends on the tissue optical properties as the Monte Carlo simulations take longer execution times for high scattering tissues and are relatively fast for low scattering media. The differences between the Monte Carlo and the Empirical approaches can be significant at larger depths and hence need to be accounted for.

3.3 Heterogeneous Brain phantom simulations (Gaussian beam)

Figure 5 shows the fluence profiles and absorption energy maps generated Monte Carlo and Empirical approach for the head phantom. The errors/differences induced by the tissue heterogeneity are seen between the two models and needs to be studied further. However it is seen that the exponential profile of the Empirical more or less follows that of the Monte Carlo. In the absorbed energy images generated in Figure 5 (b) and (c), the profile of the tumor absorption is clearly visible in the Empirical and can be demarcated within the Monte Carlo. The Monte Carlo also generates a large amount of statistical noise at larger depths which is not seen in the Empirical model. The time for execution of the Monte Carlo for a broad beam in the heterogeneous head phantom is 3.01 seconds as compared to 9 hours and 47 minutes required by the Monte Carlo. Thus the Empirical model gives a smoother approximation of the fluence profile as compared to the Monte Carlo at a fraction of the time (11701X acceleration) and thus could provide an alternative to the Monte Carlo in cases where an approximate idea of fluence distribution is needed while planning optical therapy.

4. DISCUSSION

4.1 Implications and Future Research

The current study has looked at providing an alternate voxel based approach of estimating photon fluence in 3D heterogeneous tissues besides the diffusion approximation and Monte Carlo methods. The Monte Carlo is by far the most accurate method for simulating photon deposition in tissues. However due to the large execution times, even after being implemented on parallel processing platforms, there is a need for a method for fast preliminary estimation of fluence within a certain error limit. The empirical approach is one such method which is fast and can approximate the fluence in heterogeneous tissues. By generating fluence in a 3D voxelated format, it can be easily integrated with multiple imaging modalities. More study is however necessary to understand the errors induced by the Empirical algorithm at large depths as seen in the pencil beam and broad beam fluence profiles. These errors seen can be large at depths greater than 2cm in heterogeneous phantoms. Hence the empirical approach, at this time, cannot be used for absolute quantification of photon fluence. It can however give a good approximation of the relative fluence distribution in tissues with respect to the input photon fluence. The errors in quantification can be reduced by further research into optimization methods to match the Monte Carlo. The training methodology used to derive the weights could be improved to account for the differences in the fluence profiles. Iterative routines and algorithms with merit functions can significantly enhance the accuracy of the Empirical approach.

4.2 Conclusion

The ability of the Empirical approach to approximately emulate the fluence distribution of the Monte Carlo has been studied in homogeneous and heterogeneous media. Even though the empirical algorithm cannot be used for absolute quantification, it can be used in optical therapy to evaluate the merits of different angles of illuminations and source positions which is a prerequisite for determining the placement of an optical source. The 3D GPU based Monte Carlo can then be used for absolute quantification and validation of photon energy distribution. The acceleration provided by the Empirical algorithm can be used to reduce the iterations of the Monte Carlo by identifying only a few possible illumination possibilities. Thus the Empirical algorithm has the potential to be used as a fast preliminary tool to devise optical therapies by estimating relative fluence distribution in tissues prior to validation and correction by using Monte Carlo.

REFERENCES

- [1] Mi-Ran Choi, Rizia Bardhan, Katie J. Stanton-Maxey, Sunil Badve, Harikrishna Nakshatri, Keith Stantz, Ning Cao, Naomi J. Halas, Susan E. Clare, "Delivery of nanoparticles to brain metastases of breast cancer using a cellular Trojan horse," *Cancer Nano*, 3, 47-54 (2012).
- [2] Choi MR, Stanton-Maxey KJ, Stanley JK, Levin CS, Bardhan R, Akin D, Badve S, Sturgis J, Robinson JP, Bashir R, Halas NJ, Clare SE, "A cellular Trojan Horse for delivery of therapeutic nanoparticles into tumors," *Nano Lett* 7(12), 3759–3765 (2007).

- [3] Bardhan R, Chen WX, Perez-Torres C, Bartels M, Huschka RM, Zhao LL, Morosan E, Pautler RG, Joshi A, Halas NJ, "Nanoshells with targeted simultaneous enhancement of magnetic and optical imaging and photothermal therapeutic response," *Adv Funct Mater* 19(24), 3901–3909 (2009).
- [4] Bardhan, R.; Chen, W.; Bartels, M.; Perez-Torres, C.; Botero, M. F.; McAninch, R. W.; Contreras, A.; Schiff, R.; Pautler, R. G.; Halas, N. J.; et al., "Tracking of Multimodal Therapeutic Nanocomplexes Targeting Breast Cancer In Vivo," *Nano Lett*, 10, 4920–4928 (2010).
- [5] Akshay Prabhu Verleker, Qianqian Fang, Mi-Ran Choi, Susan Clare and Keith M. Stantz, "An Optical Therapeutic Protocol to treat brain metastasis by mapping NIR activated drug release: A Pilot Study," *IEEE NSS&MIC Conf. Rec.*, M19-96 (2014), submitted for publication.**
- [6] Q. Fang and D. A. Boas, "Monte Carlo simulation of photon migration in 3D turbid media accelerated by graphics processing units," in *Opt. Express*, vol. 17, pp. 20178–20190 (2009).
- [7] N. Ren, J. Liang, X. Qu, J. Li, B. Lu, and J. Tian, "GPU-based Monte Carlo simulation for light propagation in complex heterogeneous tissues," in *Opt. Express*, vol. 18, pp. 6811–6823 (2010).
- [8] L. Wang, S. L. Jacques, and L. Zheng, "Monte Carlo modeling of light transport in multilayered tissues," in *Computer Methods and Programs in Biomedicine*, vol. 47, pp. 131–146 (1995).
- [9] D. A. Boas, J. P. Culver, J. J. Stott, and A. K. Dunn, "Three dimensional Monte Carlo code for photon migration through complex heterogeneous media including the adult human head," in *Opt. Express*, vol. 10, pp. 159–170 (2002).
- [10] Flock, S.T.; Patterson, M.S.; Wilson, B.C.; Wyman, D.R., "Monte Carlo modeling of light propagation in highly scattering tissues. I. Model predictions and comparison with diffusion theory," *Biomedical Engineering, IEEE Transactions on* vol.36, no.12, pp.1162,1168 (1989).
- [11] Beer, "Determination of the absorption of red light in colored liquids," *Annalen der Physik und Chemie*, vol. 86, 78–88 (1852).
- [12] Van der Zee, Pieter, Matthias Essenpreis, and David T. Delpy. "Optical properties of brain tissue." *OE/LASE'93: Optics, Electro-Optics, & Laser Applications in Science& Engineering*. International Society for Optics and Photonics, 1993.
- [13] M. Firbank, M. Hiraoka, M. Essenpreis, D.T. Delpy, "Measurement of the optical properties of the skull in the wavelength range 650-950 nm," *Phys. Med. Biol.*, 38, 503-510 (1993).
- [14] Cheong, Wai-Fung, Scott A. Prahl, and Ashley J. Welch. "A review of the optical properties of biological tissues." *IEEE journal of quantum electronics*, 26.12, 2166-2185 (1990).
- [15] W. M. Star, "Comparing the P3-approximation with diffusion theory and with Monte Carlo calculations of light propagation in a slab geometry," in *SPIE Proceedings on Dosimetry of Laser Radiation in Medicine and Biology*, vol. IS5, pp. 146- 154 (1989).
- [16] G. Yoon, S. A. Prahl and A. J. Welch, "Accuracies of the Diffusion Approximation and its Similarity Relations for Laser Irradiated Biological Media," in *Applied Optics*, vol. 28, pp. 2250-2255 (1989).
- [17] M. J. C. Gemert, A. J. Welch, W. M. Star, M. Motamedi, and W. F. Cheong, "Tissue optics for a slab geometry in the diffusion approximation," in *Lasers Med. Sci.*, vol. 2, pp. 295-302 (1987).
- [18] H. C. van de Hulst, "Multiple Light Scattering: Tables, Formulas, and Applications," Academic, New York, Vols. 1, 2 (1980).
- [19] R. A. J. Groenhuis, H. A. Ferwerda, and J. J. T. Bosch, "Scattering and Absorption of Turbid Materials Determined from Reflection Measurements," *Appl. Opt.* 22, 2456-2467 (1983).
- [20] S. L. Jacques and S. A. Prahl, "Modeling Optical and Thermal Distribution in Tissue During Laser Irradiation," *Lasers Surg. Med.* 6, 494-503 (1987).
- [21] J. M. Steinke and A. P. Shepherd, "Diffusion Model of the Optical Absorbance of Whole Blood," *J. Opt. Soc. Am. A* 5,813- 822 (1988).
- [22] W. M. Star and J. P. A. Marijnissen, "Calculating the Response of Isotropic Light Dosimetry Probes as a Function of the Tissue Refractive Index," *Appl. Opt.* 28, 2288-2291 (1989).

Dosimetric Validation of a Monte Carlo based Optical Planning tool

Akshay Prabhu Verleker,^{1,*} Qianqian Fang,^{2,†} Mi-Ran Choi,^{3,‡} Susan Clare,³ and Keith M. Stantz^{1,§}

¹*School of Health Sciences, Purdue University, 550 Stadium Mall Drive, West Lafayette, IN, USA*

²*Martinos Center for Biomedical Imaging, Massachusetts General Hospital,
149 13th St, Charlestown, Massachusetts, 02129, USA*

³*Department of Surgery, Feinberg School of Medicine,
Northwestern University, 303 East Superior Street, Chicago, IL 60611, USA*

compiled: September 28, 2015

A three dimensional quantification of photon energy distribution in tissues is critical in designing optical therapeutic protocols to trigger light activated drug release in tissues. The objective of this study is to develop software and dosimetry tools to simulate, characterize and cross-validate the local photon fluence in heterogeneous brain tissue, with an aim to quantify the effects of photo-activated drug release in brain tumors. A GPU enhanced voxel-based Monte Carlo code was developed to simulate the transport of near infrared photons with differing laser beam profiles (i.e., flat and super-gaussian) within phantoms of white and gray matter. From these simulations, the local photon fluence and tissue dosimetric distribution was validated through the implementation of an optical dosimetry probe with an isotropic acceptance and 1.5mm diameter. To translate these concepts into clinical practice, empirical models of photon transport were devised, calibrated to MC, and realized in CUDA to provide 3D fluence and optical dosimetric maps in real-time. These tools provide the capability to develop and optimize treatment plans for optimal release of pharmaceuticals to metastatic breast cancer in the brain. Future work will test and validate these novel delivery and release mechanisms in vivo.

1. Introduction

Optical therapy has been used extensively to treat cancer, e.g. directly in Photo Dynamic Therapy (PDT) [1] and indirectly to trigger release of drug molecules from nanocomplexes in optically targeted therapy [2, 3]. Near-infra-red (NIR) light source is preferred for deep tissue activation due to its high penetration and low optical attenuation in tissues. This study is part of a project which seeks to develop optically activated drug release in the brain and has successfully demonstrated a macrophage based Trojan Horse delivery and activation of molecules into brain metastasis [2, 3]. The broad goal is to develop an optimally targeted therapy for brain metastasis by delivering lapatinib-gold nanocomplex-laden-macrophages to metastatic lesions and optically triggering drug release, thus combining the effects of targeted drug delivery with targeted activation. With the rate/quantity of drug release being directly dependent on the optical power delivered [2, 3], a 3D Monte Carlo (MC) based protocol can be used to estimate/optimize the photon energy deposition (and subsequent drug activation) in brain tissues [10]. A fast GPU based 3D

Monte Carlo software, enhanced with a quick preliminary empirical photon propagation model can be used to devise an optimal therapeutic plan within a clinically relevant time frame. In this study we have investigated this approach and validated the Monte Carlo and the preliminary empirical model using a specially developed "linear and isotropic" optical dosimetry probe in brain tissue phantoms. The optical dosimetry probe served as the gold standard for validating the Monte Carlo model and has a better design compared to previous models.

Monte Carlo simulation has been used as the gold standard for photon propagation studies in heterogeneous media and uses probability distribution to generate the random walk of photons based on the absorption and scattering properties of tissues [4–8]. Traditional CPU based Monte Carlo models suffer from slow computation speeds, which makes them non-viable for application in clinical settings, especially in high scattering tissues (e.g. white matter). The GPU based 3D Monte Carlo (MCX model) used in this study was developed by the Fang group [9] and has been shown to have a 300X acceleration compared to the previous CPU based models. The CUDA acceleration provided by this model helps to achieve complete brain simulation of a broad beam NIR source within minutes, as compared to hours of simulation time using CPU based models [9]. Furthermore the model provides a voxel based

* Corresponding author: aprabhuv@purdue.edu

† Corresponding author: fangq@nmr.mgh.harvard.edu

‡ Corresponding author: susan.clare@northwestern.edu

§ Corresponding author: kstantz@purdue.edu

3D distribution of photon fluence and energy deposited, which can be co-registered with different medical imaging modalities (e.g. CT, MR, Ultrasound, etc), thus improving its clinical viability for diagnosis and therapy. In order to assess the effects of different illumination conditions on NIR photon distribution (and subsequent drug release) in brain tissues, we customized the Monte Carlo to emulate these user defined broad beam profiles: (a) diffuse broad beam emanating from an integrating sphere and (b) super-Gaussian beam distribution from an optical fiberguide connected to a pulsating NIR laser (wavelength 800nm). Optical brain phantoms resembling white and gray matter were designed using India ink (absorber) and Intralipid (scatterer) to resemble the absorption and scattering properties of brain tissues. The GPU based Monte Carlo was validated by comparing the MC generated fluence to localized fluence distribution measured using optical dosimetry probes. The use of a fast 3D Monte Carlo allows the development of an optical therapeutic protocol to predict photon distribution and targeted drug release in the brain in a clinically relevant timeframe [10].

Optical dosimetry is a technique of measuring localized photon distribution in tissues. Optical dosimetry probes with an isotropic response have been extensively used in photodynamic therapy (PDT) to measure photon fluence as well as to deliver light locally to tissues [1, 11, 13–16]. The small size of the dosimetry probe (1.5mm diameter) allows it to be used in localized light measurement in tissues as well as optical phantoms, unlike standard optical fluence measurement devices such as calorimeters, which cannot measure isotropic fluence and are limited by their size. In this study, we designed two types of optical dosimetry probes, with tips made of (a) titanium and (b) nylon, and evaluated their effectiveness (probe response, linearity and isotropicity) in measuring localized fluence in tissue phantoms. The titanium based dosimetry probes were found to be superior in performance, with a linear and isotropic response, compared to traditional Nylon based probes. The optical dosimetry probes were used to quantify the near infrared (NIR) photon propagation in brain tissue phantoms and validate the 3D Monte Carlo model. The dosimetry probes thus helped in calibration of the Monte Carlo software as a simulation tool to accurately predict NIR photon energy deposition in brain tissues and to emulate various light sources for clinical applications in optical therapy.

In addition to the Monte Carlo model used in this study, we designed an empirical photon propagation model to estimate photon fluence in tissues and heterogeneous media at a fraction of time taken by the GPU based Monte Carlo [17]. This Empirical approach is based on the photon convolution method and is a weight based photon propagation algorithm. This model assumes that the photon fluence in a voxel is the weighted sum of the fluences in the neighboring voxels in the preceding layer. This approach approximates

photon scatter between one layer to the next using arbitrarily assigned weights, and simulates absorption by depositing photon fluence in each voxel before proceeding to the next layer [17]. The absorption and scattering weights used in this method are calculated by comparing it to the Monte Carlo model in an 'optimization' phase (using R-square analysis). We optimized and tested the Empirical algorithm against the Monte Carlo (gold standard) for typical brain tissues such as Gray Matter, White Matter, Skull bone and Astrocytoma with known optical properties. The empirical approach can be used as a preliminary planning tool to narrow down and optimize illumination conditions for broad beams in heterogeneous brain tissues before using the more accurate Monte Carlo to estimate and optimize photon energy distribution and subsequent drug release. A targeted MC based Optical Therapeutic protocol enhanced by the Empirical approach can accurately predict and optimize photon activated drug release, while sparing healthy tissues in the brain [10].

2. Materials and Methods

2.A. Optical Brain Phantoms

Optical brain phantoms were designed to emulate the optical properties of the brain (absorption and reduced scattering coefficients), namely white matter, gray matter and skull bone at an NIR wavelength of 800nm [18, 19]. Previous studies have shown that reliable optical phantoms can be built using India ink (absorber) and intralipid (scatterer) [20–22]. India ink has a negligible scattering coefficient compared to intralipid, while absorption coefficient of intralipid is in turn negligible compared to India ink [20–22]. Thus the net scattering coefficient in the phantom is contributed by intralipid while the absorption coefficient is due to the absorption properties of India ink, in addition to the optical absorption by water molecules ($\mu_a = 0.02cm^{-1}$) [23].

The absorption coefficient of India ink (Higgins non water proof black ink), at 800nm wavelength, was determined and validated using a spectro-photometer (Shimadzu UVmini 1240 Spectrophotometer), which served as the gold standard to measure absorption. In order to measure the scattering coefficient of 20% intralipid (Intralipid 20% from Fresenius Kabi), a plexiglass cuvette filled with 20% intralipid (in various concentrations) was illuminated with a uniform NIR broad beam (wavelength 800nm) from an integrating sphere, and the attenuation coefficient measured by translating the probe along the beam axis in the solution. The attenuation coefficient measured by the probe is due to scattering by intralipid and absorption by water molecules. We then matched the probe-measured attenuation coefficient using Monte Carlo (for similar illumination conditions), by adjusting the scattering coefficient of the simulated medium. The absorption coefficient of the medium (by water molecules) was kept constant at $\mu_a = 0.02cm^{-1}$ [23]. The MC derived scattering coefficient which gave

the best match (highest R-square value) for the attenuation coefficient was selected as the derived scattering coefficient value for that concentration.

Figure 1 shows the calibration curves of concentration versus absorbance of India ink obtained using the photometer, while figure 2 shows the reduced scattering coefficient versus concentration of intralipid obtained from the Monte Carlo method. These graphs show a linear relationship between concentration and attenuation coefficient (absorption in figure 1 and scattering in figure 2) and was used to design optical phantoms with specific absorption and scattering properties to resemble white matter, gray matter and skull bone. It is important to note that the linear relationship of concentration versus attenuation can change due to miniscule (yet important) scattering properties of India ink and absorption properties of intralipid. These effects while minimal over a small range of concentrations, can be a source of uncertainties over a larger range of concentrations in phantom design. Two types of phantoms were built to resemble white and gray matter. Previous studies by Van der Zee [18] have determined the optical properties of white and gray matter, while the study by Firbank [19] determined those of skull bone. These optical properties (absorption and scattering coefficients and anisotropy factor) are shown in table 1 and were used to design the optical brain phantoms using the equations derived from figures 2 and 3.

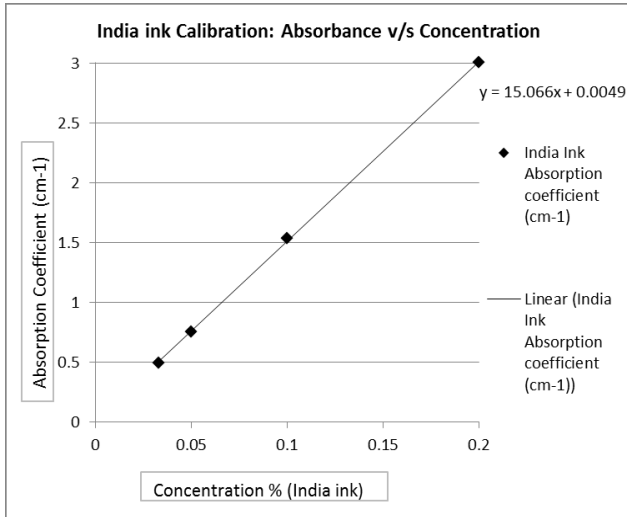


Fig. 1. Calibration curve of Spectrophotometer absorbance versus Concentration of India ink.

In order to determine the concentration of intralipid and India ink, the linear relationship of concentration versus total attenuation was used.

2.B. Dosimetry probe design and Calibration

The optical dosimetry probe consists of a spherical bulb of highly scattering material attached to an optical fiber [1, 11, 12, 14]. The optical fiber is connected to a PIN

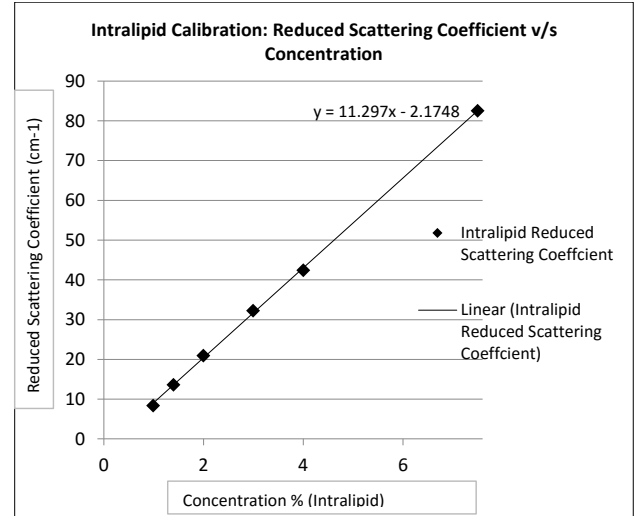


Fig. 2. Calibration curve of Reduced scattering coefficient versus Concentration of Intralipid.

Table 1. Optical Properties of Brain Tissues and Equivalent Phantom Composition [18, 19]

Tissue Type	Absorption Coefficient μ_a (cm ⁻¹)	Scattering Coefficient μ_s (cm ⁻¹)	Anisotropy Factor g	Reduced Scattering Coefficient μ_s^1 (cm ⁻¹)	Intralipid% $[\frac{\mu_s^1 + 2.1748}{11.297}]$	Ink% $[\frac{\mu_a - 0.0049}{15.066}]$
White Matter	0.05	550	0.85	82.5	7.5	0
Gray Matter	0.35	700	0.965	24.5	2.36	0.023
Skull Bone	0.24	184	0.9	18.4	1.82	0.0156

photodiode circuit whose output voltage is read using an oscilloscope. The output voltage is proportional to the optical fluence entering the spherical bulb. Two models optical dosimetry probes, with tips made of Nylon and Titanium dioxide, were designed [26]. The performance of the traditionally used Nylon based probes [14] was compared to that of the novel Titanium based probes by measuring the isotropicity of response (in equatorial and azimuthal directions) to different angles of incidence.

The Nylon spheres have been widely used for photodynamic therapy and were made of NylonTM due to their isotropic response [14]. These were used as the standard of reference to compare the performance of the novel Titanium based probes. The titanium based probes have the scattering tips made of a mixture titanium dioxide (Du Pont Ti-Pure R-900) and a clear two-part epoxy (Tra-Con BA-F114) mixed in a ratio of 9.1 mg TiO₂ to 1 ml of the epoxy (mixed) [26, 27]. The titanium probes were selected since the particle size of titanium dioxide

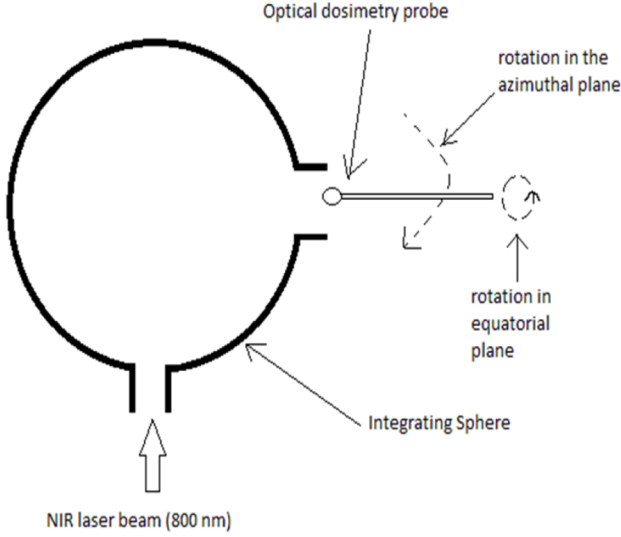


Fig. 3. Setup for calibration of the Optical dosimetry probe: measuring isotropicity (in equatorial and azimuthal planes) of the probe.

is around 410nm [27], which results in optimal scattering occurs 820nm, i.e. when the wavelength is approximately twice the particle size [27]. Since the wavelength used in our studies is 800nm, the titanium probes have been designed to show a higher sensitivity than the Nylon probes. The titanium based probe tips were molded within a specially designed mould [26] and a fiber optic cable (BFL48-400, 4mm diameter, 0.48 numerical aperture) was inserted within the cured spheres at a depth of approximately 1/3 of the sphere's radius [16]. The Nylon based probes were approximately 3.175mm diameter and were machined in a multistage process [26]. The other end of the fiber optic cable was connected to PIN photodiode (ET-2030, Electro Optics Technology Inc.) through a SMA-905 connector and the voltage output was read using an oscilloscope (Tektronix TDS3052B).

Figures 3 shows the setup used to test the isotropicity of the dosimetry probes in the equatorial and azimuthal directions. The probe tip is illuminated by laser light emanating from an integrating sphere (Melles Griot two port integrating sphere), which produces a uniform broad beam of diffuse light, which is then used to characterize the probe response. The probe is rotated at specific angles in the equatorial and azimuthal planes and its response (output rms voltage) is measured. The center of the probe tip was kept at the same location during this rotation, thus only changing its angular orientation. The isotropicity of the probe is measured by calculating its coefficient of variation, which is the ratio of standard deviation to mean of rms value over all the angles. The range of angles were 0 to 360 degrees for equatorial measurements and 0 to 150 degrees for azimuthal measurements. The angular span for Azimuthal measurements was limited due to physical limitations of

the setup (figure 4) which prevented larger angles due to presence of the integrating sphere. The individual rms voltage measured by the probe was normalized to the power measured using a calorimeter.

In the test of linearity (figure 3(A)), the dosimetry probe response is validated using a calorimeter (Ophir CE, [Nova 2 Ophir: 3A-P-SH-VI], aperture 12mm) by illuminating with a pulsed laser beam of wavelength 800 nm, frequency 10 Hz, beam intensity 10.1911 mW/cm² and energy 0.02 J/pulse. The probe and the calorimeter are translated along the beam axis (in air) and the photon fluence is measured at different positions. The linearity of response (probe v/s calorimeter) of the 1.5mm Titanium probe (selected due to its isotropicity) is shown in figure 5(B). The linearity of the probe measurement (ϕ_{probe} , mV/mm²) with respect to the calorimeter measurement ($\phi_{calorimeter}$, mV/mm²) was derived as follows by fitting a line on the measured data:

$$\phi_{probe} = \frac{\phi_{calorimeter} + 1.7296}{590.46} \quad (1)$$

The probe voltage signal was filtered using a band-pass Butterworth filter to remove high frequency noise in the probe response (figure 6). The photon fluence is proportional to integral of the probe voltage output over the time of the laser pulse and was calculated by summing over the measured voltages (in the waveform) over the pulse duration. This is a novel technique used in this study and was found to be a much better representation of the probe output as compared to measuring the absolute voltage or the root mean squared value. The probe voltage (integrated over the pulse duration) and calorimeter power were normalized to the respective surface areas [probe radius = 1.5mm, probe surface area (sphere) = 7.065mm², calorimeter aperture = 12mm, calorimeter surface area (circle) = 113.04mm²].

2.C. Absolute Photon Quantification in tissue-like media

The linear relationship in equation 1, used to quantify the photon dose in air, was modified to derive the optical fluence in liquid brain phantoms. The ratio of light entering the fiber within the probe depends on the ratio of the refractive index of the probe with respect to the medium. The refractive index of the titanium probe tip is approximately 2.73 [27] as it is made of rutile titanium dioxide. Since the refractive index of air is smaller than that of water, the probe response in water is smaller as more light leave the probe in water compared to air. The reflectance factor is 0.41 for the probe to air refractive index ratio of 2.5, and 0.74 for the probe to water ratio of 1.88 [25]. The difference in the refractive index and reflectance between probe-air and probe-water interfaces (water and tissues have similar refractive index of 1.329) must be accounted for to quantify photon dose in water. In order to determine the calibration factor we measured the probe response in air and water within a cuvette illuminated by a diffuse broad uniform beam em-

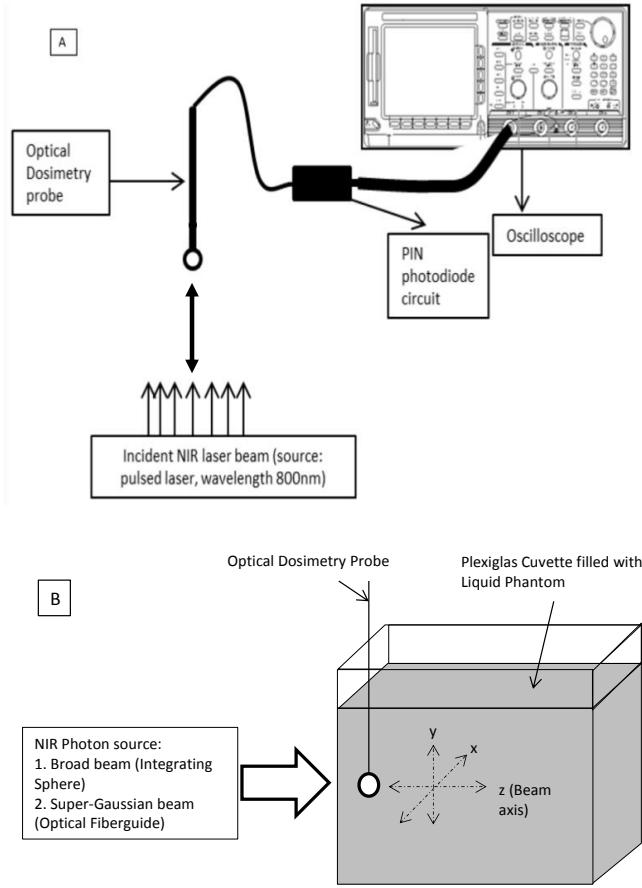


Fig. 4. (A) Setup for calibration of the Optical dosimetry probe: measuring the linearity of the probe to incident laser fluence. (B) Setup for Optical dosimetry in a liquid phantom. The optical dosimetry probe is translated within a plexiglas cuvette filled with liquid phantom, and illuminated by an NIR source. This setup is used for intralipid calibration as well as for actual phantom studies

anating from an integrating sphere (same setup as figure 3). The probe was placed inside the cuvette, 0.2cm from the surface. First the probe response voltage was measured in air (ϕ_{air}) and then measured again by filling the cuvette with water (ϕ_{water}), without changing the position of the probe with respect to the cuvette and the laser source. By accounting for the attenuation by water ($\mu_{water} = 0.02cm^{-1}$) for a pathlength (l) of 0.2cm, and the beam spread (due to change in refractive index) differences between the two setups (cuvette-to-air v/s cuvette-to-water), the calibration factor (CF) was determined experimentally to be 1.3182, using the following equation:

$$CF = \frac{\phi_{air} * (e^{(-\mu_{water} * l)}) * (\frac{fwhm_{air}}{fwhm_{water}})}{\phi_{water}} \quad (2)$$

We neglect the attenuation in air in the above calculation, and hence the probe response in air at 0.2cm from the cuvette surface is assumed to be same as that

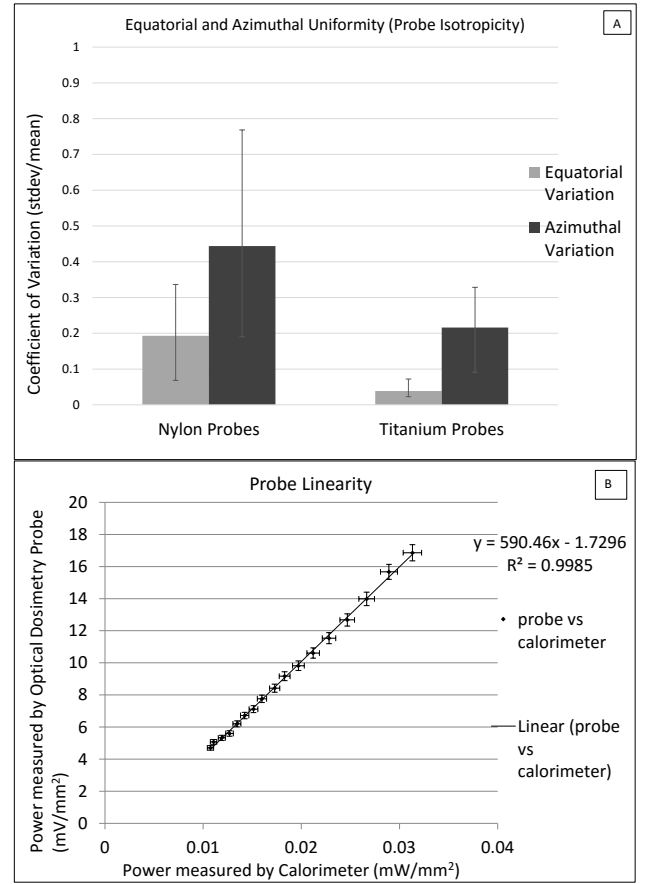


Fig. 5. (A) Probe Isotropy of Titanium v/s Nylon probes. The coefficient of variation (standard deviation/average rms voltage) was calculated for probes made of Nylon and Titanium. The error bars show indicate the minimum and maximum values of variation in individual probe response. The Titanium based probes showed a more isotropic response in the equatorial and azimuthal directions. A 1.5mm diameter Titanium probe was selected for further dosimetric studies. (B) Probe linearity: graph of total voltage (area under pulse) (mV/mm^2) measured by a 1.5mm diameter Titanium probe versus the power measured by a calorimeter per unit surface area (mW/mm^2). The probe response is linear over a dynamic range of 1.2mW to 3.5mW as measured by the calorimeter. The error bars represent 3% variation in pulsed laser power fluctuation measured by the probe and calorimeter.

at 0cm from cuvette surface (for a pathlength in air = 0.2cm). The beam spread difference between the cuvette-air setup v/s cuvette-water setup is accounted for by multiplying the fluence measured in air with the ratio of the beam spreads (or full width at half maximum fwhm) measured in the two settings. The fwhm values were measured for both these setups using the probe ($fwhm_{air}=40mm$, $fwhm_{water}=42mm$) and their ratio (0.9091) denotes the proportional change in fluence (due to beam-spread) of the laser beam between the two setups. The experimentally derived calibration factor is

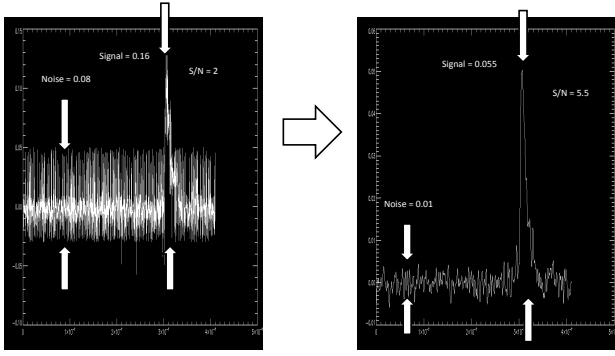


Fig. 6. Filtering the probe response using a butterworth bandpass filter. The left side shows the unfiltered signal from the probe while right hand side shows the filtered response with a high S/N ratio.

then used for absolute photon quantification by multiplying it to the probe response measured within tissues and tissue-like media (water based optical phantoms) as follows (from equation 1 and 2):

$$\phi_{absolute} = \frac{(CF * \phi_{tissue}) + 1.7296}{590.46} \quad (3)$$

Where $\phi_{absolute}$ is the absolute dose in mW/mm^2 and ϕ_{tissue} is the fluence measured by the probe (mV/mm^2) in the tissue.

2.D. Optimization of GPU based Monte Carlo

The original code of the GPU based 3D Monte Carlo (MC) was modified to emit a broad beam super-Gaussian beam profile emanating from an optical fiberguide, connected to a NIR laser. This profile was measured with a calorimeter (gold standard) and can be represented with the following equation:

$$\phi_{superGaussian} = e^{0.5 * (\frac{r}{\sigma})^n} \quad (4)$$

where

$$r = z * \tan(\theta) \quad (5)$$

Where z = perpendicular distance from the source to the plane of beam profile measurement, θ = equatorial angle subtended by a point on the beam with the plane of the source, σ = standard deviation of the super-Gaussian beam, n =order of the super-Gaussian distribution. The broad beam fiberguide output was approximated using multiple single sources with super-Gaussian outputs. In our experimental setup, a match in beam profile was obtained for $\sigma=3.8$ and $n=2.9$ for a fiberguide source of radius 0.3cm. Besides the super-Gaussian beam from the fiberguide, a flat broad beam with radius equal to the output port of the integrating sphere (port radius 0.9cm) was used to characterize the output of the integrating sphere. The beam characteristics, phantom dimensions and voxel-based optical

properties of the phantom were given as input to the MC code to emulate the illumination conditions used in the optical dosimetry setup of figure 4(B).

2.E. Validation of 3D Monte Carlo in brain phantoms using Optical dosimetry

As described in section 2.A, liquid optical phantoms, resembling white matter, gray matter and skull bone, were designed using predetermined concentrations of India ink and Intralipid. The setup for the light dosimetry in the phantoms is similar to that shown in figure 4(B). Two sources of NIR light (an integrating sphere and an optical fiberguide) were used to illuminate the phantoms, both of which were connected to the laser source (same specifications as used in the calibration process). The dosimetry probe was inserted into the phantom and translated using a calibrated translation stage to measure the optical fluence (proportional to the output voltage) distribution along x, y and z directions within the phantom. The x, y and z fluence distribution generated by the Monte Carlo was compared to the probe measurements to test the validity and accuracy of the Monte Carlo code.

In order to quantify the photon energy fluence in J/cm^2 brain tissues, we converted the output of the Monte Carlo fluence ($\phi, \text{units} : \text{photons}/\text{mm}^2$) as follows:

$$\phi_{dose}(\text{J}/\text{mm}^2) = \phi * \frac{hc}{\lambda} \quad (6)$$

Where h is planck's constant ($6.626 * 10^{-34} \text{Js}$), c and λ are the speed and wavelength of light in the medium. The energy deposited in the tissue is obtained by multiplying the photon dose with the absorption coefficient μ_a and the volume of the voxel (v):

$$\phi_{absorbed}(\text{J}/\text{mm}^2) = \phi * \mu_a * v * \frac{hc}{\lambda} \quad (7)$$

2.F. A fast Empirical algorithm for photon propagation

The Empirical approach is based on the assumption that the photon fluence in a voxel in a particular layer is a weighted sum of the fluences of neighboring voxels in the previous layer [17]. The schematic of this algorithm is shown in figure 7. The steps of the algorithm can be summarized as follows:

- 1) Assign the incident photon beam distribution (e.g. super-Gaussian beam) to the first layer of voxels. In this case, we assume that the direction of photon propagation is from layer $z=1$ to $z=\text{dim}3$.
- 2) For every voxel in a layer, calculate the 14 directional scatter components from the incident photon flu-

ence from the previous layer:

$$\begin{aligned}
I_f(x,y,z) &= I_f(x,y,z-1)wt1 \\
&+ \sum_{x-1}^{x+1} \sum_{y-1}^{y+1} (I_{fd}(x,y,z-1)wt2) \\
&+ \sum_{x-1}^{x+1} \sum_{y-1}^{y+1} (I_s(x,y,z)wt3)
\end{aligned} \tag{8}$$

$$\begin{aligned}
I_{fd}(x,y,z) &= \sum_{x-1}^{x+1} \sum_{y-1}^{y+1} (I_{fd}(x,y,z-1)wt1) \\
&+ \sum_{x-1}^{x+1} \sum_{y-1}^{y+1} (I_f(x,y,z-1)wt2) \\
&+ \sum_{x-1}^{x+1} \sum_{y-1}^{y+1} (I_s(x,y,z)wt2)
\end{aligned} \tag{9}$$

$$\begin{aligned}
I_s(x,y,z) &= \sum_{x-1}^{x+1} \sum_{y-1}^{y+1} (I_s(x,y,z)wt1) \\
&+ \sum_{x-1}^{x+1} \sum_{y-1}^{y+1} (I_{fd}(x,y,z-1)wt2) \\
&+ \sum_{x-1}^{x+1} \sum_{y-1}^{y+1} (I_f(x,y,z-1)wt3) \\
&+ \sum_{x-1}^{x+1} \sum_{y-1}^{y+1} (I_b(x,y,z+1)wt3) \\
&+ \sum_{x-1}^{x+1} \sum_{y-1}^{y+1} (I_{bd}(x,y,z+1)wt2)
\end{aligned} \tag{10}$$

$$\begin{aligned}
I_b(x,y,z) &= I_b(x,y,z+1)wt1 \\
&+ \sum_{x-1}^{x+1} \sum_{y-1}^{y+1} (I_{bd}(x,y,z+1)wt2) \\
&+ \sum_{x-1}^{x+1} \sum_{y-1}^{y+1} (I_s(x,y,z)wt3)
\end{aligned} \tag{11}$$

$$\begin{aligned}
I_{bd}(x,y,z) &= \sum_{x-1}^{x+1} \sum_{y-1}^{y+1} (I_{bd}(x,y,z+1)wt1) \\
&+ \sum_{x-1}^{x+1} \sum_{y-1}^{y+1} (I_b(x,y,z+1)wt2) \\
&+ \sum_{x-1}^{x+1} \sum_{y-1}^{y+1} (I_s(x,y,z)wt2)
\end{aligned} \tag{12}$$

$$\begin{aligned}
I_{(x,y,z)} &= I_{f(x,y,z)} + \sum (I_{fd(x,y,z)}) \\
&+ \sum (I_{s(x,y,z)}) + I_{b(x,y,z)} \\
&+ \sum (I_{bd(x,y,z)})
\end{aligned} \tag{13}$$

The 14 scatter components are: 1 forward (I_f) component, 1 backward (I_b) component, 4 side (I_s) components and 8 diagonal components (4 forward diagonals (I_{fd}) and 4 backward diagonals (I_{bd})). The arbitrary factors wt1 and wt2 are the forward and diagonal weights assigned to each directional component, which determines the percentage of scatter and the sum of all weights is always equal to one (i.e. $wt1+4wt2=1$), which only allows for redistribution of fluence (total fluence within a voxel remains same). The sum of all the scatter components in a voxel equals the total fluence in that voxel (arbitrary units: photons/unit volume).

3) Calculate absorbed fluence (I_{abs}) using Beer Lambert's law for a pathlength dl = voxel length, based on the absorption coefficient (μ_a) of the voxel:

$$I_{abs}(x,y,z) = I_{(x,y,z)} * (1 - e^{(-\mu_a * dl)}) \tag{14}$$

4) Calculate and accumulate the fluence over all voxels in the current layer and increment z to proceed to the next layer. Continue propagation till the fluence exits the volume.

The GPU based Monte Carlo was used as the golden standard to derive the weights, which depend on the reduced scattering coefficient of the medium. The weights to be assigned for scatter were obtained by an iterative optimization phase which compares the output fluence of the empirical algorithm to that generated by the Monte Carlo routine along the beam axis. The weights which show the best possible match (using highest R-square coefficient) are selected to calibrate the empirical method. Table 2 shows the weights (wt1 and wt2) obtained for a pencil beam simulation for different tissue types. The R^2 values shows the degree of match between the Monte Carlo and the Empirical method along the beam axis. The weights obtained during optimization depend on the voxel size and the scattering coefficient of the medium. The absorption coefficient is scaled to the voxel size and the photons are absorbed before proceeding to the next layer. Figure 11 shows an example of the match in fluence profiles between the Monte Carlo and the Empirical approach.

3. Results and Discussion

3.A. Optical probe calibration and photon quantification

The isotropicity (coefficient of variation) of Nylon and Titanium based optical dosimetry probes is shown in figure 5(A). The titanium based probes showed a better isotropicity with an equatorial coefficient of variation 0.0386 versus 0.1929 for Nylon probes and an azimuthal coefficient of variation of 0.216 for titanium versus 0.441

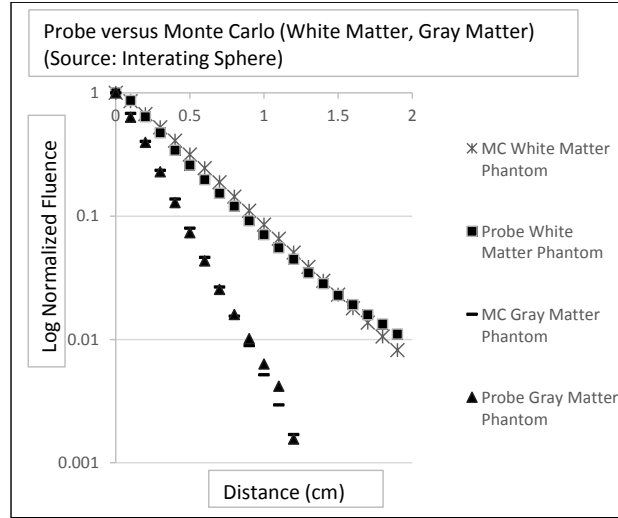


Fig. 7. Optical dosimetry in white and gray matter phantoms. The photon source used is an integrating sphere connected to a pulsating laser source. The graphs show the exponential decrease of photon fluence along the beam axis in white and gray matter mimicking phantoms. The Monte Carlo generated fluence closely matches the fluence measured by the probe.

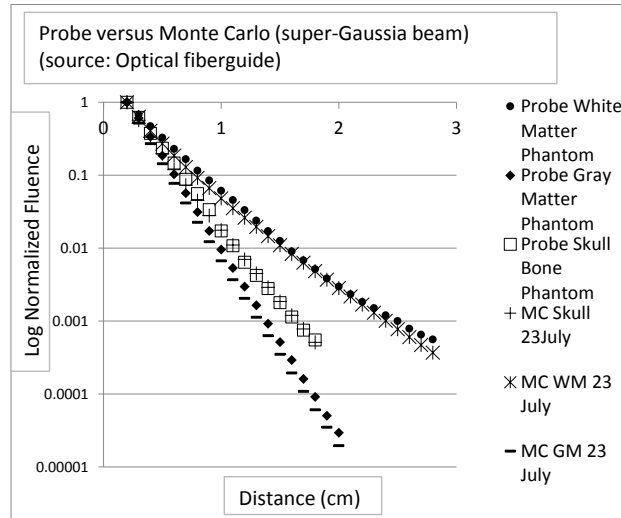


Fig. 8. Optical dosimetry in white matter, gray matter and skull bone phantoms. The photon source used is an optical fiberguide (connected to a pulsating laser source) with a super-Gaussian beam distribution. The Monte Carlo generated fluence closely matches the fluence measured by the probe. This shows that the Monte Carlo beam modeling can be reliably used as a reliable estimator of photon energy distribution in tissue phantoms.

for Nylon. A titanium based probe with a 1.5mm diameter was selected for further dosimetric studies and had an equatorial coefficient of variation of 0.0721 and an azimuthal coefficient of variation 0.2959. Figure 5(B) shows the linearity of response of the 1.5mm Titanium based probe. The probe response is linear over a dynamic range of 0.01074mW/mm² to 0.031316mW/mm² as measured by the calorimeter. The standard error (Standard Deviation/ \sqrt{n}) and percentage error variation in probe response was quantified by measuring multiple probe response in air as shown in figure 5 over

distances 10.1 to 18.1cm from the fiberguide surface. The error in probe response is 1.695% (standard error = 0.226) and the % error in calorimeter readings was 1.1299% (standard error = 0.00495). On the other hand the variation of the laser light emitted from the fiberguide over time was approximately 3%. Thus the error due to variation in pulsed optical power of the laser was the major source of error in our measurements. This showed that Titanium probes are better suited to optical dosimetry studies as compared to Nylon probes and hence were used in brain phantom studies. While Nylon

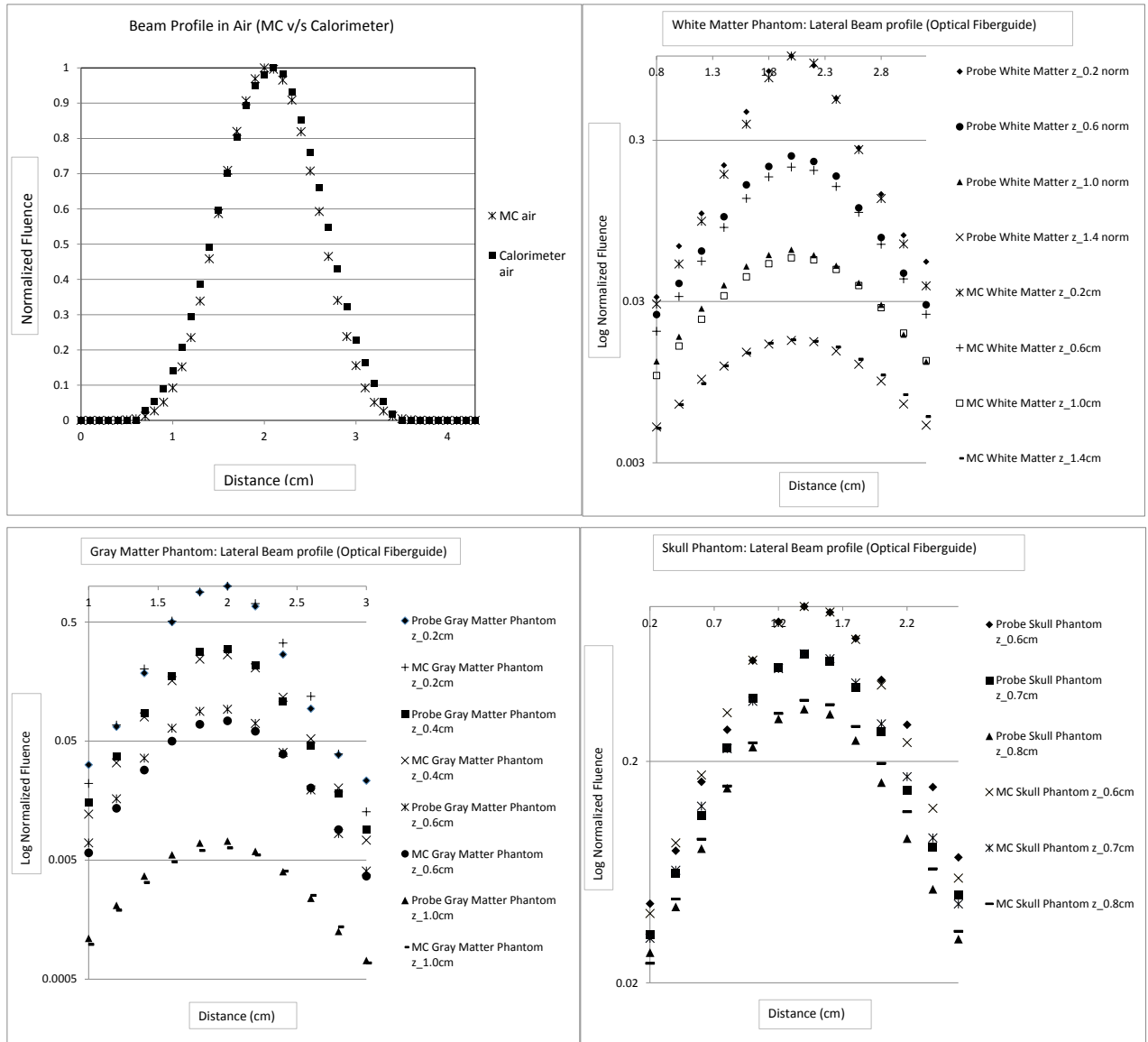


Fig. 9. Lateral beam profile measurement using optical dosimetry probe and validation by Monte Carlo. The laser source used was an optical fiberguide (0.3cm diameter) connected to a pulsed NIR laser emitting at a wavelength of 800nm. (A) Beam characterization in air using calorimeter. Optical dosimetry to measure and validate lateral beam profiles in phantoms resembling: (B) white matter, (C) gray matter and (D) skull bone, i.e., perpendicular to the beam axis. The measurements have been normalized to the maximum value measured by the dosimetry probe in each of the respective phantoms. The Monte Carlo generated fluence closely matches the fluence measured by the probe. Thus the beam spread (i.e. optical power dissipation) due can be effectively modeled using Monte Carlo.

probes have been used before in dosimetry studies, this is the first time that titanium probes were designed with a better isotropic response.

In order to calculate the absolute photon fluence in tissues and tissue-like media, the probe voltage measured within the medium must be multiplied by the calibration factor to account for the change in photon loss in the probe-medium interface with respect to the probe-air interface, where the calibration was performed. Since the refractive index of tissues is nearly same as that of

water, the calibration factor obtained for water can be used for biological media. The probe calibration factor was determined to be 1.3182. The technique presented in section 2C (using equations 1,2,3) provides a simple method to determine the calibration factor experimentally, and is a novel addition to our research. It is important to note that while equation 2 remains same for any probe, the equations 1 needs to experimentally determined, so as to derive equation 3 for absolute photon dose quantification.

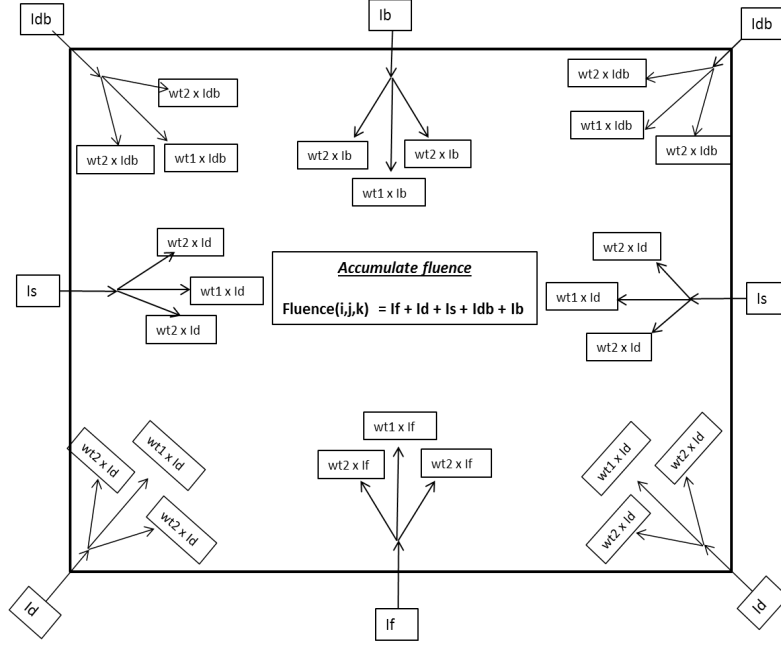


Fig. 10. Empirical method for photon propagation: The fluence at each voxel in a layer is a weighted sum of the neighboring fluences in the previous layer. The model simulates forward and diagonal scatter using arbitrarily assigned weights, derived from the Monte Carlo and which are in turn dependent on the absorption and scattering coefficients of the medium. The fluence entering a voxel is divided into 14 directional components: 1 forward, 1 backward, 4 side components, 4 forward diagonals and 4 backward diagonals.

Table 2. Optimization of Empirical algorithm

Tissue Type	Resolution (mm)	Wt1	Wt2	R^2 Coefficient
White Matter	0.1	0.95364	0.01159	1
Gray Matter	0.1	0.940728	0.014818	1
Skull Bone	0.1	0.953512	0.011622	1
Astrocytoma Tumor	0.1	0.933639	0.01659	1
White Matter	1	0.372639	0.15684	0.999916
Gray Matter	1	0.171025	0.207244	0.999905
Skull Bone	1	0.380072	0.154982	0.999919
Astrocytoma Tumor	1	0.21174	0.197065	0.999935

3.B. Optical dosimetry and Monte Carlo validation

The optical fluence measured by the dosimetry probes in white and gray matter phantoms, was compared to the Monte Carlo generated fluence. The design of optical phantoms is crucial for accurately determining the localized distribution of fluence with the probe before validating it using Monte Carlo. The optical coefficients not taken into account in this study are the miniscule scattering properties of India ink and the absorption properties of intralipid. These effects while minimal over

a small range of concentrations, can be a source of uncertainties over a larger range of concentrations in phantom design.

Figures 7 and 8 shows the comparison between the probe measurements and the Monte Carlo in brain phantoms for two different illumination profiles, flat diffuse beam (integrating sphere) and super-Gaussian (optical fiberguide) respectively. In addition to the match in the exponential direction, a comparison was also made in the direction perpendicular to the beam axis, as shown in figure 9. The plots show that the fluence measured by the probe match the Monte Carlo simulations both along and perpendicular to the beam direction. The probe measurements thus validate the 3D Monte Carlo in optical phantoms resembling brain tissues, both along and perpendicular to the beam axis, and is the major purpose of this research.

An analysis of the dose profile within the skull phantom showed that the super-Gaussian beam fluence decreases with an effective attenuation of 4.818. This factor was used to estimate the effectiveness of therapy for different skull thicknesses. Since the input photon fluence of the fiberguide is approximately 13.25mW (measured by calorimeter with aperture 12mm), the effective photon dose deposited in a skull of thickness 1cm is 0.107mW (0.0072mW/mm²), i.e. 0.808% of optical power reaches the soft tissues. On the other hand a pediatric skull of 0.5cm thickness would allow 8.99% optical power to reach the soft tissue (i.e. 0.0795mW/mm²

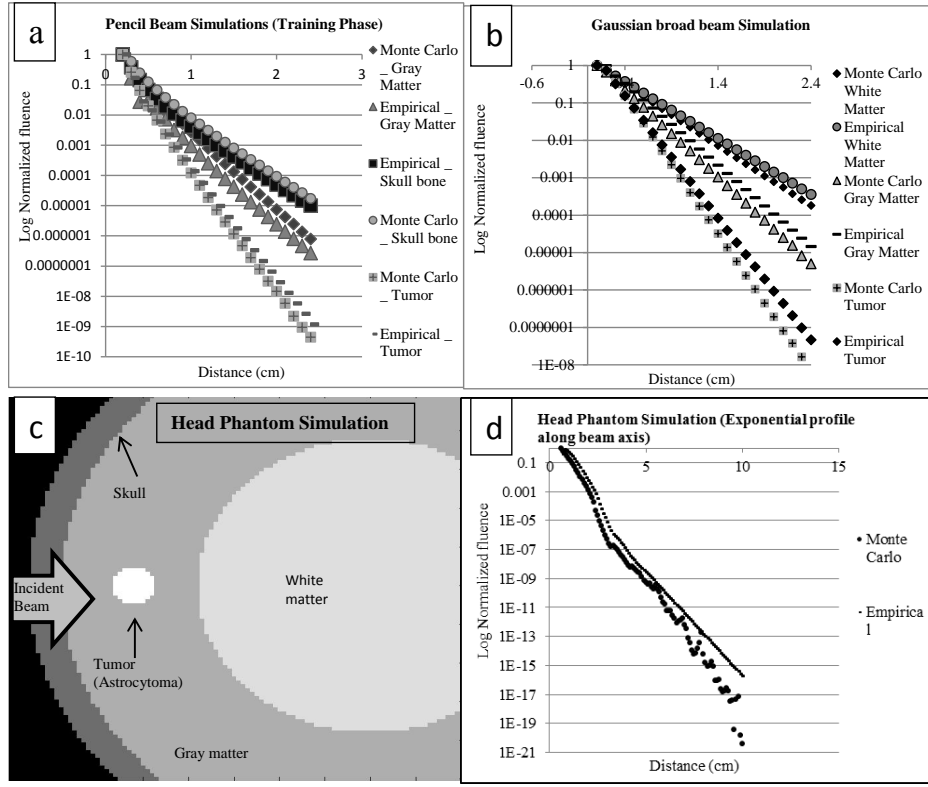


Fig. 11. Comparison of the Empirical algorithm with the Monte Carlo in homogeneous (a,b) and heterogeneous (c,d) brain phantoms resembling white matter, gray matter and astrocytoma. Part (a) shows the optimization phase using pencil beam simulations while part 2 shows exponential decrease in fluence for a Gaussian beam simulation. Part (c) shows a simulated heterogeneous brain phantom while part (d) shows fluence profiles along beam axis for the Empirical and Monte Carlo models. The empirical approach is a close approximation of the Monte Carlo over the range of optical properties of brain tissues [17].

from the fiberoptic source). The thickness of the skull and skull density determines the overall attenuation and hence an optical planning protocol needs an accurate bone density and thickness map which can be provided using a CT scan.

3.C. Empirical versus Monte Carlo

Figure 11 shows the comparison between the Monte Carlo and Empirical in brain tissues for both pencil and broad beam simulations in homogeneous and heterogeneous phantoms. Figure 11(a) shows the results for pencil beam simulations, 11(b) shows comparison using Gaussian beams while 11(d) shows the comparison in a heterogeneous simulated head phantom as shown in 11(c), with the optical properties described in table 1. The weights derived from the optimization phase for pencil beams were used in the broad beam simulations (figures 11(c) and 11(d)). The fluence generated by the Monte Carlo closely matches the empirical fluence in both homogeneous and heterogeneous brain tissue phantoms along the beam axis.

The Monte Carlo code is computationally expensive in spite of being based on a GPU based platform. In order to simulate the optical properties and fine structural boundaries of brain tissues, we need a fine resolu-

tion equal to or less than 1mm. An optical map of the brain can be obtained through segmenting and translating CT and/or MR images into corresponding optical properties. With such tiny resolutions, the CT dataset size of the brain becomes very large (for example a CT dataset of size 512x512x512 matrix with 0.625mm resolution and 160mm collimation). This significantly increases the execution time of the Monte Carlo routine to iterate over various illumination conditions and to simulate photon propagation through a large dataset in every iteration. The Empirical approach provides an alternative means to replace the computationally expensive Monte Carlo, for preliminary analysis by reducing the execution time to select the best illumination conditions for therapy. The acceleration achieved by the Empirical algorithm was approximately 700X for a pencil beam simulation and 16000X for a broad beam simulation in a head phantom.

4. Conclusions

This study validates the 3D fluence distribution simulated by a Monte Carlo, using an optical dosimetry probe in phantoms resembling white matter, gray matter and skull bone. The use of a dosimetry probe with a better design, i.e., with a linear and highly isotropic response,

allowed for accurate localized measurement of NIR photon fluence in tissue phantoms ($< 1\%$ error), and further increased the accuracy of the measurements. The probes themselves were calibrated using calorimeter gold standard and a unique calibration factor was derived specific to the probe. The 3D validation of the Monte Carlo generated fluence for two different types of NIR light sources in different optical phantoms, and the ease of photon quantification to absolute dose (in mW/mm^2 or J/mm^2) proves the fidelity of the Monte Carlo as a predictive tool to accurately estimate 3D photon energy distribution in complex media. The prediction error of the Monte Carlo is determined by the 3% variation of optical power and $< 1\%$ error of the calorimeter/dosimetry probe setup. The voxelated structure of the medium to be simulated allows the Monte Carlo to emulate complex geometrical shaped of tissues by accepting datasets generated by other imaging systems (e.g. CT/MRI) and without any pre-knowledge of tissue geometries, unlike previous versions of the Monte Carlo. This, along with the flexibility of generating user defined photon beams proves adaptability of the Monte Carlo to be used in clinical studies as a predictive tool to estimate photon dose distribution in heterogeneous brain tissues.

The empirical approach provides a robust and fast means of assessing the tissue illumination and its weights are obtained through the optimization phase with the Monte Carlo. The acceleration provided by the Empirical algorithm increases the clinical feasibility of optical therapeutic planning to narrow down the complex possibilities of illumination conditions, further compounded by the heterogeneous structure of the brain (e.g. varying skull thicknesses and densities). One disadvantage of using the Empirical approach is that the weights assigned depend on the resolution of the medium and changing resolution requires an optimization phase to derive the weights. In spite of its limitations and optimization requirements, the Empirical can provide an acceleration over the Monte Carlo to analyze complex illuminations via iterative routines and in preliminary studies to determine the best irradiation angles. The empirical approach can thus be used as a preliminary step prior to using the Monte Carlo, with the final analysis (final estimation) being done by the Monte Carlo to ensure high therapeutic accuracy to ensure drug release.

Our ultimate goal is to design a fast Monte Carlo based optical therapeutic protocol to treat brain metastasis. This requires voxel by voxel determination of photon energy distribution to accurately predict the rate/quantity of drug release. This study achieves the first step of designing such a tool to validate the NIR photon distribution in three dimensions in optical phantoms. The next step will be to test Monte Carlo in predicting photon distribution in heterogeneous tissue samples and under various illuminations beam profiles. The tissue structure and boundaries can be determined using other imaging modalities such as MRI or CT scan to separate various tissue types and obtain an optical

property map of the tissue sample. This can be used an input to the Monte Carlo to obtain photon distribution in the tissue sample.

References

- [1] Marijnissen JPA, Star WM, van Delft JL, Pranken NAP. Light intensity measurements in optical phantoms and in vivo during HPD-photoradiation treatment, using a miniature light detector with isotropic response. In: Jori G, Perria C (eds) Photodynamie therapy of tumours and other diseases. Padova: Libreria Progetto, (1985):387-90.
- [2] Choi MR, Stanton-Maxey KJ, Stanley JK, Levin CS, Bardhan R, Akin D, Badve S, Sturgis J, Robinson JP, Bashir R, Halas NJ, Clare SE. "A cellular Trojan Horse for delivery of therapeutic nanoparticles into tumors." *Nano Lett* 7(12) (2007): 37593765.
- [3] Mi-Ran Choi, Rizia Bardhan, Katie J. Stanton-Maxey, Sunil Badve, Harikrishna Nakshatri, Keith Stantz, Ning Cao, Naomi J. Halas, Susan E. Clare. "Delivery of nanoparticles to brain metastases of breast cancer using a cellular Trojan horse." *Cancer Nano* 3 (2012): 47-54.
- [4] W. M. Star. Comparing the P3-approximation with diffusion theory and with Monte Carlo calculations of light propagation in a slab geometry. in *SPIE Proceedings on Dosimetry of Laser Radiation in Medicine and Biology*, vol. IS5, (1989): 146- 154.
- [5] G. Yoon, S. A. Prahl and A. J. Welch. "Accuracies of the Diffusion Approximation and its Similarity Relations for Laser Irradiated Biological Media." in *Applied Optics*, vol. 28, (1989): 2250-2255.
- [6] M. J. C. Gemert, A. J. Welch, W. M. Star, M. Motamedi, and W. F. Cheong. Tissue optics for a slab geometry in the diffusion approximation, in *Lasers Med. Sci.*, vol. 2, (1987): 295-302.
- [7] L. Wang, S. L. Jacques, and L. Zheng, "Monte Carlo modeling of light transport in multilayered tissues." *Computer Methods and Programs in Biomedicine*, vol. 47, (1995): 131-146.
- [8] D. A. Boas, J. P. Culver, J. J. Stott, and A. K. Dunn. Three dimensional Monte Carlo code for photon migration through complex heterogeneous media including the adult human head. in *Opt. Express*, vol. 10, (2002): 159170.
- [9] Q. Fang and D. A. Boas. "Monte Carlo simulation of photon migration in 3D turbid media accelerated by graphics processing units." *Opt. Express*, vol. 17, (2009): 20178-20190.
- [10] Akshay Prabhu Verleker, Qianqian Fang, Mi-Ran Choi, Susan Clare and Keith M. Stantz. "An Optical Therapeutic Protocol to treat brain metastasis by mapping NIR activated drug release: A Pilot Study." *IEEE NSS/MIC Conf. Rec.*, M19-96 (2014), submitted for publication.**
- [11] Marijnissen JP, Star WM. "Phantom measurements for light dosimetry using isotropic and small aperture detectors." *Prog Clin Biol Res.*, 170:133-48 (1984).
- [12] Van Staveren, H., et al., "Construction, quality assurance and calibration of spherical isotropic fibre optic light diffusers. *Lasers Med Sci*, (1995). 10(2): p. 137147.
- [13] Driver I, Lowdell C P and Ash D V. "In vivo measurement of the optical interaction coefficients of human tu-

- mours at 630 nm." *Physics in medicine and biology* 36 (1991): 805-13.
- [14] Marijnissen, J. P. A., and W. M. Star. "Calibration of isotropic light dosimetry probes based on scattering bulbs in clear media." *Physics in medicine and biology* 41.7 (1996): 1191.
 - [15] Star, Willem M. "Light dosimetry in vivo." *Physics in medicine and biology* 42.5 (1997): 763.
 - [16] Marijnissen, J. P. A., and W. M. Star. "Performance of isotropic light dosimetry probes based on scattering bulbs in turbid media." *Physics in medicine and biology* 47.12 (2002): 2049.
 - [17] Verleker, Akshay Prabhu, Qianqian Fang, Mi-Ran Choi, Susan Clare, and Keith M. Stantz. "An empirical approach to estimate near-infra-red photon propagation and optically induced drug release in brain tissues." In *SPIE BiOS, International Society for Optics and Photonics*, (2015): pp. 93080T-93080T.
 - [18] Van der Zee, Pieter, Matthias Essenpreis, and David T. Delpy. "Optical properties of brain tissue." *OE/LASE'93: Optics, Electro-Optics, and Laser Applications in Science and Engineering*. International Society for Optics and Photonics, (1993).
 - [19] M. Firbank, M. Hiraoka, M. Essenpreis, D.T. Delpy. "Measurement of the optical properties of the skull in the wavelength range 650-950 nm," *Phys. Med. Biol.*, 38 (1993):503-510.
 - [20] Madsen, Steen J., Michael S. Patterson, and Brian C. Wilson. "The use of India ink as an optical absorber in tissue-simulating phantoms." *Physics in medicine and biology* 37.4 (1992): 985.
 - [21] Driver, I., et al. "The optical properties of aqueous suspensions of Intralipid, a fat emulsion." *Physics in medicine and biology* 34.12 (1989): 1927.
 - [22] Flock, Stephen T., et al. "Optical properties of Intralipid: a phantom medium for light propagation studies." *Lasers in Surgery and Medicine* 12.5 (1992): 510-519.
 - [23] Irvine, William M., and James B. Pollack. "Infrared optical properties of water and ice spheres." *Icarus* 8.1 (1968): 324-360.
 - [24] Cheong, Wai-Fung, Scott A. Prahl, and Ashley J. Welch. "A review of the optical properties of biological tissues." *IEEE journal of quantum electronics* 26.12 (1990): 2166-2185.
 - [25] Orchard SE. "Reflection and transmission of light by diffusing suspensions" *J. Opt. Soc. Am.* 59 (1969): 1584-97.
 - [26] Shaffer M. "Dynamic Contrast Enhanced Photoacoustic Computed Tomography in MDA-MB-231 and BT-474 Xenograft Tumor Models," PhD Thesis, Purdue University (2012), 54-67.
 - [27] DuPont Titanium Technologies, Titanium Dioxide for Coatings. Coatings selection brochure P200067, (2002): Wilmington, DE.